Modelling and
Simulation in Materials
Science and
Engineering

TOPICAL REVIEW • **OPEN ACCESS**

A review of level-set modeling in epitaxial growth and alloys solidification

To cite this article: Frederic Gibou *et al* 2026 *Modelling Simul. Mater. Sci. Eng.* **34** 013001

Modelling and Simulation in Materials Science and Engineering

TOPICAL REVIEW

A review of level-set modeling in epitaxial growth and alloys solidification

Frederic Gibou[1,2,*], **Ron Fedkiw**[3], **Russel Caflisch**[4] and **Stanley Osher**[5]

[1] Department of Mechanical Engineering, University of California, Santa Barbara, CA 93106, United States of America
[2] Department of Computer Science, University of California, Santa Barbara, CA 93106, United States of America
[3] Department of Computer Science, Stanford University, Stanford, CA 94305, United States of America
[4] Courant Institute of Mathematical Sciences, New York University, New York, NY 10012, United States of America
[5] Department of Mathematics, University of California, Los Angeles, CA 90095, United States of America
[*] Author to whom any correspondence should be addressed.

E-mail: fgibou@ucsb.edu, rfedkiw@stanford.edu, caflisch@courant.nyu.edu and sjo@math.ucla.edu

Keywords: level-set, computational materials, metal additive manufacturing, solidification, epitaxy

OPEN ACCESS

RECEIVED
13 June 2025

REVISED
25 October 2025

ACCEPTED FOR PUBLICATION
8 January 2026

PUBLISHED
28 January 2026

Abstract

Level-set methods provide a powerful computational framework for simulating free boundary problems in materials science. This paper presents a unified perspective on their application to two distinct phenomena: multicomponent alloy solidification and epitaxial island growth. Although these problems differ significantly in physical mechanisms and characteristic length scales, they can both be effectively addressed within the level-set framework, highlighting the versatility of the method across diverse applications. We outline the mathematical formulations and highlight computational advances and common features across applications. This overview highlights the role of level-set methods as a foundational tool in predictive materials modeling.

1. Introduction

The level-set method of Osher and Sethian [1] has emerged as a versatile computational framework for simulating interface dynamics. Its implicit representation of interfaces allows it to naturally handle topological changes and to impose sharp boundary conditions at the exact location of the interface with controlled accuracy. The level-set method has had tremendous success in diverse fields. In fluid dynamics, it has been widely employed to model a broad spectrum of multiphase flow phenomena. Representative applications include two-phase and free-surface flows [2–7], Hele–Shaw flows and incompressible flows in complex geometries [8, 9], compressible detonation dynamics [10], droplet–surface interactions, and coupled problems involving fluid–solid or incompressible–compressible interfaces [11–13]. The level-set method has also made a significant impact in image processing. For instance, level-set-based feature-preserving techniques have been developed to smooth noisy surfaces, in a manner closely related to diffusion-based image processing methods [14]. Comprehensive overviews of these approaches can be found in the book and review articles on the subject [15, 16]. In computer graphics, the level-set method has been widely adopted to simulate complex fluid–structure interactions, including the two-way coupling between fluids and thin deformable solids such as cloth or rigid shells [17]. It has also been employed to generate highly realistic animations of water dynamics [18–21], as well as to capture the visual complexity of phenomena such as flames [22] and bubbles [23]. The level-set method has also found extensive application in problems of optimization and shape reconstruction. Notable examples include its use in inverse problem techniques for the design of photonic crystals [24], the reconstruction of surfaces from point clouds [25], and the optimization of geometries under constraints [26]. It has further been employed to determine optimal shapes for structural design [27, 28] and to reconstruct solvent-excluded surfaces of large biomolecules [29, 30]. Beyond these applications, the level-set method has been applied to problems in self-assembly of diblock copolymers, including the solution of inverse

problems that identify confinement geometries guiding block copolymer assembly toward prescribed target patterns in lithography [31–36]. A broader overview of level-set approaches for inverse problems and optimal design can be found in [37].

Hybrid strategies have also been investigated, where the level-set method is coupled with other interface-tracking techniques, such as volume-of-fluid or particle-based methods, to enhance accuracy and mass conservation [38–40]. For comprehensive perspectives, the reader is referred to several key reviews and monographs on the subject [41–44]. In the field of materials science, these developments have enabled the formulation of sophisticated models for processes governed by evolving free boundaries, thereby extending the versatility of the level-set method to a wide range of technologically relevant phenomena.

This paper presents a unified perspective on the application of level-set methods to two distinct, yet thematically linked, problems in materials science:

1. The modeling of solidification in multicomponent alloys in the context of additive manufacturing (AM) using a sharp-interface formulation.
2. The modeling of epitaxial growth using an island dynamics model (IDM).

These applications differ in scale and governing physics, yet benefit from the level-set method's strengths in capturing evolving interfaces. Level-set methods have been applied to many other applications in materials and we refer the interested reader to [45] and the references therein. Taken together, these applications demonstrate the breadth and robustness of level-set methods in modeling free boundary problems that differ significantly in physical mechanisms and characteristic length scales. This review brings together these perspectives and highlights the method's contribution to advancing predictive simulation capabilities in materials science.

1.1. Alloy solidification

AM holds immense promise for the development of advanced engineering components, particularly through its unique ability to fabricate complex three-dimensional geometries that would be difficult or impossible to achieve using conventional manufacturing techniques. Beyond geometric flexibility, AM also enables site-specific control over material properties by tuning processing parameters and thermal histories at a localized scale [46–51]. This capability opens new pathways for the design and optimization of performance-critical parts in aerospace, biomedical, and energy systems. Recent studies have demonstrated the potential of AM to tailor microstructure and phase distribution during fabrication, thereby enhancing strength, ductility, and fatigue resistance in targeted regions of a component [46–51].

Realizing the full potential of AM requires a fundamental understanding of the complex, multiphysics phenomena (heat transfer, mass diffusion, and fluid flow) that occur during solidification and how they influence the resulting microstructures and properties. Key features such as solute segregation, grain morphology, crystallographic orientation distribution, and defect formation (e.g. pores and cracks) are governed by the conditions at the solid–liquid interface during the melt pool evolution. Among the most critical solidification parameters are the local interface velocity (R) and the thermal gradient (G), which can span several orders of magnitude within a single melt pool and vary spatially and temporally during processing.

Designing AM-processed materials with targeted microstructures and properties therefore demands predictive models that can map solidification regimes (planar, cellular, columnar, and equiaxed growth) onto the (G, R) space for specific alloy systems. Although several models exist to predict structural transitions, such as the columnar-to-equiaxed transition [52, 53], they often rely on empirical parameters that are difficult to measure or estimate experimentally and were originally developed under unidirectional growth conditions, which are not representative of AM melt pool environments. As a result, these models frequently lack predictive capability under the complex thermal conditions imposed by scanning strategies and beam parameters. There remains a significant knowledge gap linking thermal transport, fluid flow, solute redistribution, and microstructure evolution, especially in multicomponent alloy systems.

In response to this need, a wide range of numerical strategies have been developed to simulate solidification. These approaches generally fall into three categories: cellular automata (CA) methods [54], phase-field or other diffuse-interface methods [55–58], and sharp-interface methods [59–65]. CA methods are computationally efficient but are rule-based rather than physics-based, limiting their fidelity. Phase-field methods offer a rigorous continuum approach in which the solid–liquid interface is described

by a diffuse transition zone. However, while phase-field theory is asymptotically convergent to sharp-interface descriptions in the limit of vanishing interface thickness, practical implementations require artificially broadened interfaces, which may reduce accuracy for highly localized phenomena. To the best of our knowledge, there is currently no phase-field approach that can consider more than ternary systems. Considering a diffuse interface has also been considered within the level-set method [58], using the level-set method to track the interface but solving transport equations using smeared boundary conditions. This approach has the advantage of being simple but only approximately satisfies boundary conditions such as the Gibbs–Thomson relation.

Sharp-interface methods, on the other hand, explicitly model the solid–liquid boundary as a discontinuity. While they require sophisticated algorithms for interface tracking and for enforcing boundary conditions, they offer the advantage of faithfully representing the true macroscale physical description. In the case of a pure substance, where only the temperature field is solved, the early application of the level-set method was introduced by [66], who employed a boundary integral formulation to compute the temperature. This was later followed by the work of [59], who solved the temperature equation directly on a grid. In [59], the boundary condition at the interface was implemented using the method of Mayo [67], resulting in a second-order accurate scheme but yielding a non-symmetric linear system. Subsequently, [68] proposed a symmetric discretization of the problem, which was later extended to a fourth-order accurate scheme (albeit again producing a non-symmetric system) in [69]. This line of work was further extended in [62] to adaptive grids, achieving second-order accuracy for both the temperature field and its gradient in the context of the diffusion equation, and resulting in a fully second-order accurate method for pure substances. The level-set methodology was later extended to binary systems in [64, 65].

Truly sharp-interface simulations have been largely limited to binary alloys, leaving a gap in modeling capabilities for more realistic multicomponent systems. This gap has recently been addressed in [70], where a sharp-interface computational framework for multicomponent alloy solidification was introduced. The model couples temperature evolution, solute diffusion, and interface motion, capturing the complex interplay of physical phenomena at the solid–liquid boundary. Key physical effects, including crystallographic anisotropy, capillarity, and solute rejection, are resolved discretely as macroscopic discontinuities, rather than through approximate smoothing. A distinctive feature of the model is its use of thermodynamically consistent, composition-dependent liquidus slopes and partition coefficients, obtained from the PANDAT^{TM} database, allowing accurate representation of local equilibrium at the interface.

Numerically, the framework leverages adaptive mesh refinement (AMR) on quadtree grids and is optimized for scalable performance on parallel computing architectures. This allows for physically realistic simulations under thermal conditions characteristic of AM, such as high cooling rates and steep temperature gradients. The approach has been demonstrated on the solidification of Co–Al–W alloys, a ternary system relevant to structural applications, and has considered simulation of a penta-alloy. To the best of our knowledge, this work represents the first sharp-interface computational engine capable of simulating solidification in alloys with an arbitrary number of alloying elements.

1.2. Epitaxial growth

Epitaxial growth underlies the fabrication of many modern electronic and optoelectronic devices, ranging from transistors and quantum dot lasers to advanced memory architectures and catalysts, by enabling the controlled deposition of atoms and molecules onto heated substrates, where they assemble into crystalline layers with atomic-scale precision [71–74]. The resulting structures exhibit extremely low defect densities, which are essential for device performance. However, simulating this process is challenging because the involved length and time scales span many orders of magnitude, from submonolayer atomic events to surface morphology evolution across lateral scales of several microns or more. This disparity necessitates multiscale modeling frameworks that span atomistic, mesoscale, and continuum descriptions [75, 76]. A comprehensive theoretical framework must accurately describe atomistic phenomena such as surface diffusion, nucleation, and island coalescence, as well as the transition to multilayer growth regimes, which can result in kinetic roughening. The morphology of the growing film is sensitive to experimentally tunable parameters such as the ratio of the surface diffusion constant D to the deposition flux F, which governs whether atoms integrate smoothly into existing islands or form new nucleation sites. Capturing these mechanisms in a model that is both quantitatively predictive and computationally feasible across multiple regimes is a significant challenge [77, 78]. Ideally, such a model should be applicable to a wide range of homoepitaxial and heteroepitaxial systems, compatible with various growth techniques, and capable of resolving dynamic processes from atomic to device scales. Level-set simulations

offer a powerful framework for studying these effects by bridging atomistic processes and continuum-scale behavior, making them particularly promising for the development of tools for engineering applications in advanced materials design.

Kinetic Monte Carlo (KMC) methods have long been a central tool for studying epitaxial growth, as they directly incorporate atomistic event rates derived from fundamental physical principles, thereby providing a natural framework for mimicking the underlying microscopic processes. Historically, one of the earliest applications of KMC to epitaxial growth was the work of [79], who developed a fast KMC algorithm for simulating molecular beam epitaxy. This contribution was instrumental in demonstrating that stochastic event-driven methods could efficiently capture deposition, diffusion, and nucleation processes central to epitaxial layer formation. Since then, KMC has become the standard approach for simulating epitaxial phenomena across a wide range of material systems. For example, [80] introduced a multiscale KMC algorithm specifically tailored for epitaxial growth, demonstrating how stochastic atomistic events can be systematically coupled with larger-scale morphological evolution. Earlier, [81] provided a comprehensive review of KMC simulations in the context of chemical vapor deposition, highlighting the versatility of the method in describing growth processes involving adsorption, diffusion, and reaction kinetics. In turn, [82] applied first-principles-based KMC simulations to heterogeneous catalysis, offering a paradigm for how physically rigorous event rates can yield predictive insights into complex surface processes. Recent advances highlight both the flexibility and the continuing relevance of KMC to contemporary materials science. For example, [83] applied large-scale KMC simulations to the epitaxial growth of graphene, providing insight into how growth kinetics and nucleation influence the morphology of two-dimensional materials. Their results underscore the ability of KMC to address the challenges of simulating extended time and length scales in emerging low-dimensional systems. Likewise, [84] used KMC to investigate the influence of growth conditions on the epitaxial growth of 3C–SiC(0001) vicinal surfaces. Their study illustrates the predictive power of KMC in technologically important heteroepitaxial systems, where temperature, flux, and miscut angle strongly affect step-flow dynamics and surface morphology.

Collectively, these studies illustrate how KMC serves as a bridge between fundamental atomic-scale mechanisms and experimentally observable growth behavior. At the same time, despite their accuracy and physical fidelity, KMC simulations are computationally demanding, particularly when long-range interactions or extended spatiotemporal scales must be resolved, posing challenges for their application to larger systems or technologically relevant growth regimes. By contrast, level-set simulations provide a continuum-based alternative that efficiently bridges atomistic mechanisms with mesoscale and continuum-scale behavior. The level-set formulation enables a continuous representation of island boundaries, even as these coalesce, shrink, or evolve anisotropically. The IDM [85–87], developed in this framework, offers a continuum alternative to KMC simulations, efficiently capturing stochastic nucleation and interface motion via deterministic adatom flux at the islands' boundaries. A key advantage of the IDM and its level-set formulation is its significantly lower computational cost compared to Monte Carlo simulations when accounting for long-range interactions such as elastic forces arising from lattice mismatch.

1.3. Outline

Section 2 provides an overview of the level-set method, the core numerical algorithms on which it is based, and how boundary conditions are imposed in this implicit approach. Sections 3 and 4 present applications of the method to multicomponent alloy solidification and epitaxial growth, respectively. Finally, section 5 offers concluding remarks and discusses future research directions.

2. The level-set method

The level-set method, introduced by Osher and Sethian [1], represents a moving interface as the zero level set of a higher-dimensional scalar function. The interface evolves implicitly under a velocity field determined by the governing physical laws, allowing for natural handling of topological changes such as merging and pinching. The level-set function $\phi(\mathbf{x})$ is set to be negative in one phase (e.g. the liquid phase in a solidification process) that occupies the region denoted Ω^- and positive in the other phase (e.g. the solid phase in a solidification process) that occupies the region denoted Ω^+:

$$\phi(\mathbf{x}) < 0, \forall \mathbf{x} \in \Omega^-, \quad \phi(\mathbf{x}) = 0, \forall \mathbf{x} \text{ on } \Gamma, \quad \phi(\mathbf{x}) > 0, \forall \mathbf{x} \in \Omega^+.$$

Figure 1 illustrates the level-set methodology for free-boundary problems. In this framework, the governing physical equations are solved in the regions Ω^- and Ω^+, while appropriate boundary conditions are prescribed on the evolving interface Γ. The procedure for imposing boundary conditions

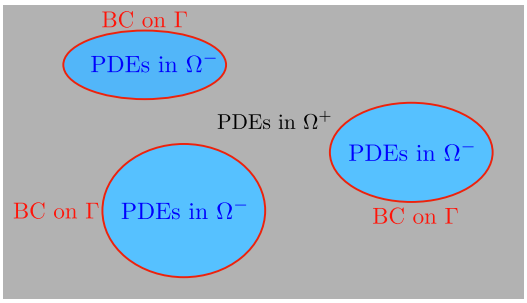

Figure 1. Typical level-set setup to free boundary problems.

within the level-set framework is presented in section 2.3, and the sets of partial differential equations governing each region are detailed in section 3 for solidification and section 4 for the IDM.

Although in principle the level function can be chosen to be any Lipschitz continuous function, a practical choice is to define the level-set function as the signed distance to the interface Γ. As the level-set function is deformed under its normal velocity, it is necessary to re-initialize it to a signed distance function. When the normal velocity exhibits strong anisotropy, it is necessary to perform the reinitialization procedure at every time step in order to maintain the signed-distance property. More generally, carrying out reinitialization at each step is a sound rule of thumb in scientific applications. A traditional approach is to solve the *reinitialization* equation [2]:

$$\phi_\tau + \text{sign}\left(\phi^0\right)\left(|\nabla\phi| - 1\right) = 0, \tag{1}$$

where τ is a pseudo-time step, taken in practice to correspond to a number of iterations between 10 and 15.

In materials science, this representation proves especially useful in problems where the interface dynamics depend on coupled processes such as diffusion, reaction kinetics, phase transformations, or mechanical deformation. The method's ability to maintain a sharp interface and its compatibility with structured or adaptive grids make it particularly well-suited for high-resolution simulations. In addition, the level-set representation provides a straightforward way to compute the normal vector, $\boldsymbol{n}$, to the boundary and its mean curvature, κ:

$$\boldsymbol{n} = \frac{\nabla\phi}{|\nabla\phi|}, \qquad \kappa = \nabla\cdot\boldsymbol{n} = \nabla\cdot\frac{\nabla\phi}{|\nabla\phi|}.$$

Given the normal velocity of the interface, $v_{\boldsymbol{n}} = \boldsymbol{v}\cdot\boldsymbol{n}$, derived from physical models, the level-set function is evolved under using the level-set equation:

$$\frac{\partial\phi}{\partial t} + v_{\boldsymbol{n}}|\nabla\phi| = 0. \tag{2}$$

2.1. Discretization of the level-set equations

2.1.1. Spatial discretization

The discretization of the normal and curvature are straightforward and are based on simple central differencing. The discretizations of the reinitialization equation (1) and the level-set equation (2) are more involved and are based on numerical advances on Hamilton–Jacobi solvers, themselves based on advances in computational methods for conservation laws. Since those equations can be solved in a dimension-by-dimension approach, it is enough to present the approach in one spatial dimension.

The Hamilton–Jacobi equation in one spatial dimension is written as:

$$\phi_t + H(\phi_x, x, t) = 0, \tag{3}$$

and its discretization takes the form:

$$\phi_i^{n+1} = \phi_i^n - \Delta t H_i^n\left(\phi_x^-, \phi_x^+\right),$$

where ϕ_x^-, ϕ_x^+ are the approximation of the left and right derivative of the level-set function ϕ^n and H_i^n is an approximation of the Hamiltonian H.

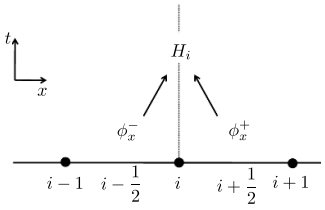

Figure 2. Framework for defining the numerical Hamiltonian H_i^n.

The first difficulty when considering numerically approximating the level-set equations is the fact that equations are nonlinear and therefore can produce shock and rarefaction solutions that require approximating derivatives of functions with steep gradients or kinks. Issued from progress made in the context of conservation laws, the schemes used are of the type Essentially Non-Oscillatory (ENO)/Weighted Essentially Non-Oscillatory (WENO) [88–91]. The main idea behind those approaches is to create a customized stencil at each grid point in order to approximate derivatives, with the driving principle being to start from the standard upwind direction and add grid points to the stencil in such a way as to avoid regions of sharp gradients; sharp gradients can conveniently be estimated by creating a finite difference table at each grid point. The ENO/WENO schemes used in these studies are detailed in appendix.

Remarks:

1. We note that the use of ENO/WENO schemes, compared to a first-order upwind discretization, inevitably increases the computational cost by a factor of three to four, depending on the sophistication of the implementation. However, such high-order schemes are essential to mitigate the excessive numerical diffusion associated with simple upwinding, which would otherwise compromise the accuracy of the solution to the point of rendering the results unreliable.
2. In the case of uniform grids, the WENO scheme is typically used. In the case of adaptive grids, given the computational cost of accessing grid points that are not immediately in the neighborhood of a grid point at which we are seeking an approximation of the derivatives, we are limiting the ENO procedure to second-order accuracy in conjunction with the treatment of T-junction nodes described in section 2.2.

The second difficulty is to properly approximate, at each grid point, the Hamiltonian H_i^n depending on the values of ϕ_x^-, ϕ_x^+ (see figure 2). This approximation must take into account nonlinear effects related to shocks and rarefaction waves, following the Godunov strategy that defines the Hamiltonian as follows:

$$H_i^n \approx \begin{cases} \min\limits_{\phi_x \in [\phi_x^-, \phi_x^+]} H(\phi_x), & \text{if } \phi_x^- \leqslant \phi_x^+, \\ \max\limits_{\phi_x \in [\phi_x^+, \phi_x^-]} H(\phi_x), & \text{if } \phi_x^- \geqslant \phi_x^+. \end{cases} \tag{4}$$

For example, in the case of the level-set equation (2), which can be re-written as follows to give a direct handle on the characteristic directions:

$$\phi_t + \frac{v_n \phi_x}{\sqrt{\phi_x^2 + \phi_y^2 + \phi_z^2}} \phi_x + \frac{v_n \phi_y}{\sqrt{\phi_x^2 + \phi_y^2 + \phi_z^2}} \phi_y + \frac{v_n \phi_z}{\sqrt{\phi_x^2 + \phi_y^2 + \phi_z^2}} \phi_z = 0,$$

the Godunov formula, gives the following discretization for the term ϕ_x term:

1. If $v_n \phi_x^- \leqslant 0$ and $v_n \phi_x^+ \leqslant 0$ discretize ϕ_x by ϕ_x^+.
2. If $v_n \phi_x^- \geqslant 0$ and $v_n \phi_x^+ \geqslant 0$ discretize ϕ_x by ϕ_x^-.
3. If $v_n \phi_x^- \leqslant 0$ and $v_n \phi_x^+ \geqslant 0$ set $\phi_x = 0$.
4. If $v_n \phi_x^- \geqslant 0$ and $v_n \phi_x^+ \leqslant 0$
   (a) If $|v_n \phi_x^+| \geqslant |v_n \phi_x^-|$ discretize ϕ_x by ϕ_x^+.
   (b) If $|v_n \phi_x^+| \leqslant |v_n \phi_x^-|$ discretize ϕ_x by ϕ_x^-.

The terms ϕ_y and ϕ_z are discretized similarly, the results are plugged into equation (2). The reinitialization equation is discretized almost identically by writing equation (1) as:

$$\phi_\tau + \text{sign}\left(\phi^0\right)\left(\frac{\phi_x}{\sqrt{\phi_x^2+\phi_y^2+\phi_z^2}}\phi_x + \frac{\phi_y}{\sqrt{\phi_x^2+\phi_y^2+\phi_z^2}}\phi_y + \frac{\phi_z}{\sqrt{\phi_x^2+\phi_y^2+\phi_z^2}}\phi_z - 1\right) = 0.$$

2.1.2. TVD-RK3

The spatial discretization is traditionally coupled with a TVD-RK3 algorithm for the time evolution [88]. TVD stands for Total Variation Diminishing and can be written as a set of simple Euler steps in combination with linear averaging of the solution at intermediate steps. In the case of the Hamilton–Jacobi equation (3), we start from ϕ^n, and perform one Euler step to find a temporary $\tilde{\phi}^{n+1}$ at each grid point:

$$\frac{\tilde{\phi}_i^{n+1} - \phi_i^n}{\Delta t} + H_i^n = 0,$$

followed by another Euler step to find a temporary $\tilde{\phi}_i^{n+2}$:

$$\frac{\tilde{\phi}_i^{n+2} - \tilde{\phi}_i^{n+1}}{\Delta t} + H_i^{n+1} = 0,$$

where H_i^{n+1} is computed using equation (4) with ϕ_x^-, ϕ_x^+ computed from $\tilde{\phi}^{n+1}$. Once $\tilde{\phi}^{n+2}$ is found, we apply a weighted averaging procedure to find a temporary $\tilde{\phi}^{n+\frac{1}{2}}$:

$$\tilde{\phi}_i^{n+\frac{1}{2}} = \frac{3}{4}\phi_i^n + \frac{1}{4}\tilde{\phi}^{n+2}.$$

Last, another Euler step is used to find a temporary $\tilde{\phi}_i^{n+\frac{3}{2}}$:

$$\frac{\tilde{\phi}_i^{n+\frac{3}{2}} - \tilde{\phi}_i^{n+\frac{1}{2}}}{\Delta t} + H_i^{n+\frac{1}{2}} = 0,$$

where $H_i^{n+\frac{1}{2}}$ is computed using equation (4) with ϕ_x^-, ϕ_x^+ computed from $\tilde{\phi}^{n+\frac{1}{2}}$. The updated solution ϕ^{n+1} at each grid point is defined by a weighted average: ϕ^{n+1}:

$$\phi_i^{n+1} = \frac{1}{3}\phi_i^n + \frac{2}{3}\tilde{\phi}_i^{n+\frac{3}{2}}.$$

We also refer the interested reader to other methodologies to reinitialize the level-set function that are not based on partial differential equation (PDE) evolution equations, such as the Fast Marching Method [42, 92, 93], the Fast Sweeping Method [94, 95] and their parallel versions [96–98], or other explicit approaches [99–103], as well as the recent work by Osher seeking to overcome the curse of dimensionality [104, 105] for Hamilton–Jacobi equations.

2.2. Adaptive grid refinement

The level-set method is known to exhibit a form of numerical error commonly referred to as 'mass loss,' wherein the evolving interface deviates slightly from the expected physical trajectory. This artifact, however, diminishes with grid refinement and results in a negligible loss of mass when sufficiently fine grids are used. Because the computational cost scales with the number of grid points and high resolution is primarily needed in the vicinity of the interface, AMR presents a particularly effective strategy. In addition, many problems in materials science are either diffusion-dominated or governed by partial differential equations with parabolic or elliptic components. These equations typically yield smooth solutions, except near interfaces where discontinuities or sharp gradients may arise. This further supports the use of adaptive grids, which concentrate computational resources where they are most needed while minimizing overall cost. An example of a three-dimensional crystal growth simulation is presented in figure 4.

In the context of AMR, quadtree and octree data structures representation of adaptive Cartesian grids offer optimal efficiency in terms of both memory usage and CPU cost. In [107], the authors proposed a straightforward discretization strategy applicable to level-set methods [108], parabolic and elliptic equations in irregular domains [61, 62, 109–116], as well as the Navier–Stokes equations [117]. The core contribution lies in the treatment of T-junction grid points, which are points on the grid where one (in

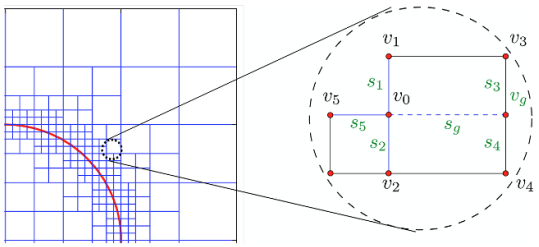

Figure 3. Zoom on a T-junction grid point.

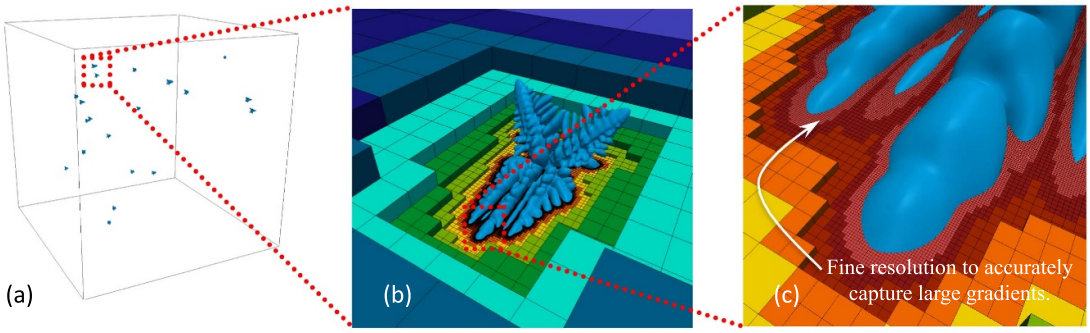

Figure 4. Simulation of crystal growth in 3D (a) with a zoom on one crystal (b) and a further zoom on the resolved thermal boundary layer (c). Figure reprinted from [106], Copyright (2016), with permission from Elsevier.

2D) or two (in 3D) neighboring grid points are missing, as illustrated in figure 3. The authors introduced a definition for these missing neighbors that enables third-order accuracy:

$$u^G = \frac{s_4 u_3 + s_3 u_4}{s_3 + s_4} - \frac{s_3 s_4}{s_1 + s_2}\left(\frac{u_2 - u_0}{s_2} + \frac{u_1 - u_0}{s_1}\right).$$

This formulation allows the use of standard upwind or central differencing schemes as if the grid were uniform, while maintaining the desired level of accuracy. We note that given the computational cost of accessing grid points that are not immediately in the neighborhood of a grid point at which we are seeking an approximation of the derivatives, we are limiting the ENO procedure to second-order accuracy. We note that adaptive grids are particularly advantageous for elliptic and parabolic problems, i.e. those dominated by diffusion. In such cases, the solution is infinitely smooth away from the interface and can therefore be accurately resolved on relatively coarse grids. Near the interface, however, discontinuities in the solution and/or its flux require enhanced resolution, which can be efficiently provided by local grid refinement. For example, [118] demonstrated that an adaptive grid with a coarse 32×32 background resolution achieves the same level of accuracy as a uniform 256×256 grid, provided that the grid is locally refined to the effective 256×256 level within a narrow band around the interface. Building on the `p4est` library [119], which manages the distribution of adaptive grids across multiple processes, [106] developed the `casl` library, which implements level-set methods and standard solvers optimized for massively parallel architectures. Additional work utilizing the octree data structure includes that of [19, 21] and research on mainly compressible flows on AMR can be found in [120] and the references therein.

2.3. Imposing boundary conditions

An important advantage of the level-set method lies in its ability to impose sharp boundary conditions, namely, the capability to enforce conditions directly at the precise interface location with controlled accuracy (see sections 2.3.1–2.3.3), while preserving the discontinuities in the solution and its flux. This capability is particularly important when modeling systems under the continuum assumption underpinning conservation laws, where rapid variations across physical interfaces are accurately represented as sharp discontinuities rather than smooth transitions. Boundary conditions typically fall into Dirichlet, Robin (with a sub case being Neumann) and jump conditions. In the context of solidification, the Gibbs–Tompson is a well-known Dirichlet physical boundary condition that describes the equilibrium temperature of the phase transition and the concentration of alloying elements have a jump across

Figure 5. Example of a typical numerical solution of the Poisson equation with jump conditions on irregular domains. Figure reprinted from [129], Copyright (2020), with permission from Elsevier.

the solidification front. An example of Robin boundary condition will be discussed in the context of epitaxy (section 4) that is responsible for mound formation.

The Ghost Fluid Method (GFM), originally introduced to capture sharp discontinuities in compressible flow and detonation problems [121–124], has significantly influenced how sharp boundary conditions are imposed within the level-set framework. In the context of compressible flows, the central idea is to track the location of shocks and contact discontinuities using the level-set method, while maintaining two separate numerical solutions; one on each side of the interface representing the real fluid, and a ghost fluid that is defined as the real fluid plus the Rankine–Hugoniot jump condition. Thanks to the definition of a ghost fluid, the solution remains continuous across the interface and therefore avoids directly differentiating discontinuous functions, thereby eliminating the large numerical errors that would otherwise arise.

This simple yet powerful approach has been successfully extended to elliptic and parabolic problems. In particular, it has been applied to the Poisson and diffusion equations on irregular domains with Dirichlet boundary conditions, as well as to problems involving jump conditions. In this section, we briefly describe the methodology for jump, Dirichlet and Robin/Neumann conditions.

2.3.1. Jump boundary conditions

In the case of elliptic and parabolic equations, the jump conditions are given for the solution u and its flux $\nabla u \cdot \boldsymbol{n}$, in the form $[u] = f$ and $[\mu \nabla u \cdot \boldsymbol{n}] = g$, respectively, where $f = f(x,t)$ and $g = g(x,t)$ are known functions, μ is a variable coefficient (e.g. the thermal conductivity in a solidification problem), the 'jump operator' of a quantity Q is defined by $[Q] = Q^+ - Q^-$, where $Q^{+/-}$ is the value of Q at the interface on the $\Omega^{+/-}$ side, and the unit normal $\boldsymbol{n}$ points towards the inside of Ω^-.

The first Ghost-Fluid approach replaced the jump in flux by its projection to each spatial dimension, resulting in a strategy that is simple since it allows a dimension-by-dimension approach to approximating the Laplace operator [125]. In the case where the tangential component of the jump in flux are crucial, this approach may introduce a numerical smearing of the tangential components that can pollute the solution. To address this limitation, three techniques have been proposed. The first, inspired by the work of [126], uses a Voronoi partition so that the degrees of freedom of the Voronoi cell are orthogonal to their edges, making the application of the approach of [125] accurate when tangential terms are important [127]. The second, known as xGFM [128], extends the GFM by enforcing the full jump condition in the normal direction through an iterative process.

The third approach, introduced in [129], constructs second-order accurate expressions for the solution on either side of the interface using normal derivatives of the solution. The difference between these expressions is then directly linked to the jump conditions in the solution and its flux. By approximating the local gradient via a least-squares fit using neighboring points, this method yields two candidate formulas for the ghost value. Interestingly, [129] observe that choosing the formula corresponding to the region with the smaller diffusion coefficient leads to a linear system with significantly improved conditioning. Figure 5 is an example of the imposing sharp jump conditions using the method of [129], illustrating that the jumps in the solution and its flux are indeed imposed at the discrete level. As illustrated in figure 6, both the condition number and the numerical error in the solution and its gradient remain well-controlled (i.e. bounded), even in the presence of strong discontinuities in the diffusion coefficient. We recall that for a linear system of equations $Ax = b$, the condition number, $\kappa(A)$, measures

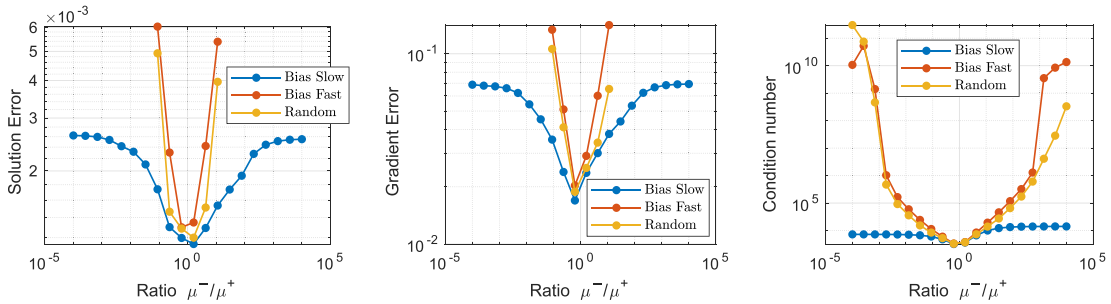

Figure 6. `Conditioning test` in two spatial dimensions (each data point represents the maximum value among $10 \times 10 = 100$ different relative placements of an immersed interface on the computational grid). Figure reprinted from [129], Copyright (2020), with permission from Elsevier.

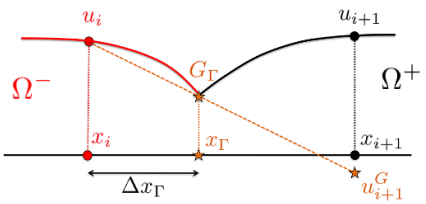

Figure 7. Definition of the ghost value u^G_{i+1} using a linear extrapolation. First, construct a linear interpolant $I(x) = ax + b$ of u such that $I(0) = u_i$ and $I(\Delta x_\Gamma) = u_\Gamma$. Then define $u^G_{i+1} = I(\Delta x)$.

how sensitive the solution of the linear system is to small errors in the input b. A high condition number indicates that significant accuracy may be lost when solving the linear system (roughly up to $\kappa(A)\,\varepsilon$, where ε is machine precision). The condition numbers is therefore a useful measure to assess the reliability of the solution of a linear system of equations. From a practical point of view, it is necessary to use the method in [129] to avoid smearing in the tangential component. We note, however, that for some applications such as incompressible flows without phase change nor Marangoni effects, tangential components are absent, and the approach of [125] can be employed instead, which is simpler to implement. In both cases, the resulting scheme achieves second-order accuracy in the maximum norm.

2.3.2. Dirichlet boundary conditions

Solving elliptic or parabolic problems requires implicit discretizations, where a linear system of equations is built. Specifically, each line of the linear system is filled with the coefficients of the standard central differencing formula in each spatial direction. In cases where a specific value must be imposed on an irregular domain, the typical configuration is illustrated in figure 7, where the solution exhibits a discontinuity in the derivative at the interface[6]. The GFM addresses this by defining a ghost value that still enables the use of standard central differencing while preserving the sharp interface behavior. This ghost value is defined by considering the extrapolation of the solution from one side of the interface to the other, which in turn gives the modified coefficients of the linear system for grid points adjacent to the interface. The order of accuracy and the symmetry of the linear system is detailed in [68, 69, 130] summarizes which extrapolation to use depending on the problem considered.

2.3.3. Robin boundary conditions

Robin boundary conditions are commonly employed to model physical phenomena such as convective heat or mass exchange at boundaries, semi-permeable membranes, imperfect insulation, or radiative transfer, among many. In its most general form, Robin boundary conditions are written as $\dfrac{\partial u}{\partial \boldsymbol{n}} + \alpha\, u = g$, where $\alpha = \alpha(\boldsymbol{x}, t)$ and $g = g(\boldsymbol{x}, t)$ are given functions; in the case where $\alpha = 0$ the boundary condition is of Neumann type. Robin boundary conditions are important as they give a condition for the flux of the solution across the free boundary. An example of such application is given in section 4 for the simulation of mounding in epitaxial growth.

[6] In the case where, in addition, the solution itself is discontinuous, the numerical treatment outlined in section 2.3.2 is identical as it fully decouples the numerical solution on both sides of the interface.

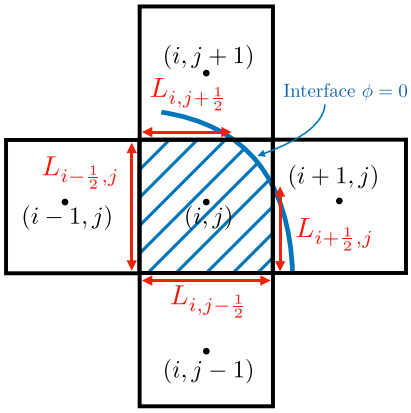

Figure 8. Local grid arrangement of a computational cell centered at (i, j) cut by an interface defined by the level-set function ϕ.

Although finite difference approaches extending the Ghost-Fluid Method for Dirichlet conditions of [68, 69], have been adapted to impose Robin boundary conditions within the level-set framework [131–136], a finite volume approach is generally preferred due to its more natural incorporation of boundary fluxes and compatibility with conservative formulations. Through the use of the divergence theorem over each cell containing the zero-level set (see figure 8), the boundary condition is naturally incorporated into the formulation, reducing the problem to computing fluxes across the boundary of the computational cell and the integration of a known function over the zero-level of the level-set function. Specifically, the discretization of the Laplace operator over a computational cell $C_{i,j}$, covered by the irregular domain Ω, is treated as follows:

$$-\Delta u = f \iff -\int_{C_{i,j}\cap\Omega} \Delta u \, dC = \int_{C_{i,j}\cap\Omega} f \, dC$$
$$\iff -\int_{\partial C_{i,j}\cap\Gamma} \nabla u \cdot \boldsymbol{n} \, dC = \int_{C_{i,j}\cap\Omega} f \, dC.$$

The right-hand side of the last equality is approximated as $f_{i,j} \times \text{Area}(C_{i,j} \cap \Omega)$, whereas the left-hand side of the last equality can be approximated as:

$$-L_{i+\frac{1}{2},j}\frac{u_{i+1,j}-u_{i},j}{\Delta x} - L_{i-\frac{1}{2},j}\frac{u_{i,j}-u_{i-1,j}}{\Delta x}$$
$$-L_{i,j+\frac{1}{2}}\frac{u_{i,j+1}-u_{i,j}}{\Delta x} - L_{i,j-\frac{1}{2}}\frac{u_{i,j}-u_{i,j-1}}{\Delta x} - \int_{\Gamma}(g-\alpha u)\, d\Gamma,$$

where the $L_{i\pm\frac{1}{2},j\pm\frac{1}{2}}$ represent the length of the portion of the cell faces covered by the irregular domain (see figure 8). Imposing Robin boundary conditions therefore boils down to approximating the integral of $(g-\alpha u)$ over an interface represented by the level-set function.

The first finite volume formulation of Robin boundary conditions within the level-set framework was introduced in [137], where the numerical integration of $(g-\alpha u)$ was based on the geometric approach developed in [113, 138, 139]. This method is second-order accurate in the maximum norm. We are not aware of alternative approaches for imposing Robin boundary conditions that achieve a comparable balance of simplicity and accuracy for interfaces that do not develop kinks. This methodology was subsequently extended to support adaptive grids and moving interfaces in [61]. While this approach produces symmetric linear systems that are desirable for their fast inversion using standard linear algebra numerical methods, the solution gradient is only first-order accurate. In turn, this limits free boundary problems to first-order accuracy if they depend on the solution gradient; typical examples in materials are those considered here. To solve that problem, [140] extended the work of [137] to produce second-order accurate solutions, albeit non-symmetric linear systems, where one of the main ingredients is the evaluation of the fluxes between cells that are discretized using the ideas of [141]. The methodology was then extended in [142] to the case where the boundary is piece-wise continuous, i.e. applicable to the case where the interface itself has kinks. The method retains second-order accuracy in the maximum norm, including on adaptive grids and in the presence of kinked interfaces, and thus constitutes the most advanced available approach.

3. Application—solidification of multicomponent alloys in AM

3.1. Sharp interface model

Consider the solidification of an alloy system composed of $N+1$ chemical species: a dominant solvent element that forms the primary matrix of the alloy, and N additional solute elements present in lesser concentrations. Such multicomponent alloy systems are representative of many technologically important materials, including high-entropy alloys and advanced superalloys, where the interactions between multiple solute elements and the solvent play a critical role in determining microstructural evolution during solidification. The thermodynamic and kinetic complexities introduced by the presence of multiple solutes (including solute partitioning, cross-diffusion effects, and non-linear phase equilibria) make the modeling and control of solidification processes in these systems particularly challenging. Accurate description of these phenomena is essential for predicting phase selection, morphology development, and segregation patterns, which ultimately govern the mechanical and functional properties of the solidified material.

We denote the evolving solid–liquid interface by $\Gamma(t)$, and define the domains within the computational domain Ω that are occupied by the solid and liquid phases as Ω^s and Ω^l. We also define the temperature, at time t and location $\boldsymbol{x}$, as $T = T(t,\boldsymbol{x})$ and the N different compositions as $C^J = C^J(t,\boldsymbol{x})$, $J \in [1,N]$ in the solid and liquid regions as:

$$T(t,\boldsymbol{x}) = \begin{cases} T^l(t,\boldsymbol{x}), & \boldsymbol{x} \in \Omega^l(t) \\ T^s(t,\boldsymbol{x}), & \boldsymbol{x} \in \Omega^s(t) \end{cases}, \quad \text{and} \quad C^J(t,\boldsymbol{x}) = \begin{cases} C_J^l(t,\boldsymbol{x}), & \boldsymbol{x} \in \Omega^l(t) \\ C_J^s(t,\boldsymbol{x}), & \boldsymbol{x} \in \Omega^s(t) \end{cases}, \quad J \in [1,N].$$

In the absence of convective transport, the evolution of thermal and solutal fields is governed by diffusion-dominated processes. The energy and species conservation laws reduce to classical diffusion equations within each phase:

$$\rho^\nu {c_p}^\nu \partial_t T^\nu - \lambda^\nu \nabla^2 T^\nu = 0, \qquad \boldsymbol{x} \in \Omega^\nu(t), \quad \nu = s,l, \tag{5}$$

$$\partial_t C_J^\nu - D_J^\nu \nabla^2 C_J^\nu = 0, \qquad \boldsymbol{x} \in \Omega^\nu(t), \quad \nu = s,l, \qquad J \in [1,N], \tag{6}$$

where, ρ^ν, ${c_p}^\nu$, and λ^ν denote the mass density, specific heat capacity, and thermal conductivity, respectively, within each phase $\nu \in s,l$, corresponding to solid and liquid states. Similarly, D_J^ν represents the diffusivity of the J^{th} solute species in phase ν. The domains $\Omega^s(t)$ and $\Omega^l(t)$ evolve over time due to phase transformation at the solid–liquid interface.

For the sake of clarity and tractability, we assume constant material properties within each phase, i.e. ρ^ν, ${c_p}^\nu$, λ^ν, and D_J^ν are considered independent of temperature and composition. Although more sophisticated models may account for their dependence on local thermodynamic conditions, this simplification is often adequate for capturing the essential features of diffusion-driven solidification dynamics, and the resulting equations provide the foundation for more advanced models incorporating interface kinetics, interfacial energy effects, and thermodynamic equilibrium conditions at the moving boundary. It is also important to note that in the context of multicomponent alloy solidification, it is standard practice to solve the energy conservation equation in both the liquid and solid phases, as thermal diffusion occurs at comparable timescales in both regions. In contrast, the governing diffusion equations for the chemical species are generally restricted to the liquid phase, a modeling choice that is justified by the fact that solute diffusion in the solid is several orders of magnitude slower than in the liquid and can, to a good approximation, be neglected over the solidification timescale. Consequently, the solid is often treated as a stationary phase with respect to solute transport, which simplifies the computational model without compromising accuracy. This assumption is widely adopted in the literature and forms the basis of many sharp-interface and phase-field models of alloy solidification.

In the modeling of multicomponent alloy solidification, the temperature and concentration fields must satisfy a series of thermodynamic and interfacial conditions at the evolving solid–liquid interface. A fundamental assumption in this framework is that the phase transformation occurs at local thermodynamic equilibrium. Consequently, the temperature field is continuous across the solidification front, leading to the condition:

$$[T] = 0, \quad \text{on } \Gamma(t), \tag{7}$$

where the jump operator $[\cdot]$ represents the difference in a field variable across the interface (i.e. $[T] = T^s - T^l$, with T^s and T^l denoting the temperatures on the solid and liquid sides, respectively). Furthermore, the temperature at the interface must satisfy a generalized Gibbs–Thomson condition that

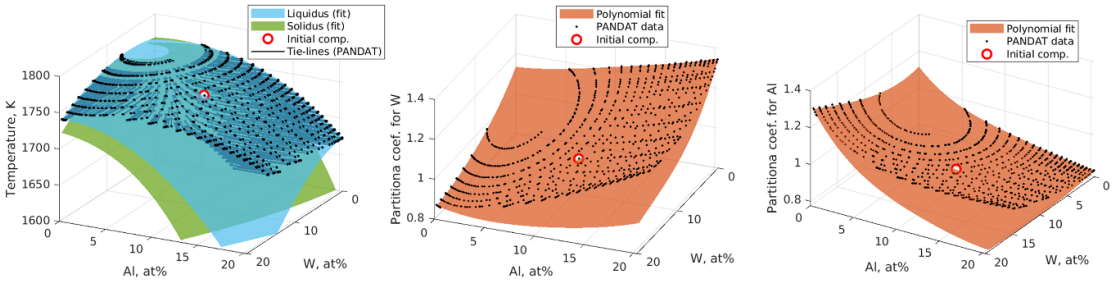

Figure 9. Phase-diagram of Co–W–Al as predicted by the PANDAT™ database (dots) and polynomial approximations (solid surface) used in this work. Figure reprinted from [70], Copyright (2023), with permission from Elsevier.

accounts for both interface kinetics and curvature effects:

$$T^I = T^{\text{liq}}(C_1, \ldots, C_N) + \epsilon_v(\boldsymbol{n})\, v_{\boldsymbol{n}} + \epsilon_c(\boldsymbol{n})\, \kappa, \quad \text{on } \Gamma(t), \tag{8}$$

where $T^{\text{liq}}(C_1, \ldots, C_N)$ defines the local liquidus temperature as a function of the solute concentrations. The normal velocity of the interface is denoted $v_{\boldsymbol{n}}$, and κ represents the mean curvature of the interface, while $\epsilon_v(\boldsymbol{n})$ and $\epsilon_c(\boldsymbol{n})$ are the kinetic and capillary coefficients, respectively, which may depend on the orientation of the interface normal $\boldsymbol{n}$.

In classical solidification models, the liquidus temperature is often approximated as a linear function of composition:

$$T^{\text{liq}}(C_1, \ldots, C_N) = T_m + m_1 C_1 + \ldots + m_N C_N,$$

where T_m is the melting temperature of the pure solvent, and m_J are referred to as the liquidus slopes for the solutes $C_1, \ldots, C_N$. However, such linear approximations are insufficient for capturing the thermodynamic complexity of multicomponent alloys, where interactions between solutes can lead to highly nonlinear behavior in the phase diagram. To address this, [70] adopted a more general approach by allowing the liquidus temperature T^{liq} to be an arbitrary, composition-dependent, function. Accordingly, the liquidus slopes $m_J = \partial T^{\text{liq}}/\partial C_J$ are treated as functions of the local composition, enabling a more accurate and physically realistic description of the solidification process. For the numerical simulations reported in [70], the necessary thermodynamic data are obtained from the PANDAT™ database, which provides reliable multicomponent phase equilibria for engineering alloys (see figure 9).

The thermal and chemical conditions at the solid–liquid interface play a critical role in determining the morphology and composition of the resulting microstructure. The thermal balance at the moving interface is governed by a Stefan-type condition, which enforces the conservation of energy by equating the net heat flux across the interface to the latent heat released or absorbed during the phase transition:

$$[\lambda \partial_{\boldsymbol{n}} T] = v_{\boldsymbol{n}} L_f, \quad \boldsymbol{x} \in \Gamma(t), \tag{9}$$

where L_f denotes the latent heat of fusion per unit volume, λ is the thermal conductivity, $\partial_{\boldsymbol{n}} T$ is the temperature gradient normal to the interface, and $v_{\boldsymbol{n}}$ is the normal velocity of the interface. This condition ensures that the local thermal field responds dynamically to the evolving interface and accommodates the release or absorption of latent heat associated with phase change.

In addition to thermal equilibrium, chemical equilibrium must be maintained at the solidification front. For multicomponent systems, this is typically captured through the concept of partition coefficients k_J, which describe the equilibrium distribution of each solute species between the solid and liquid phases. These coefficients are defined as:

$$C_J^s = k_J C_J^l, \quad \boldsymbol{x} \in \Gamma(t), \quad J \in [1, N],$$

where C_J^l and C_J^s are the concentrations of species J in the liquid and solid phases, respectively. Importantly, for general multicomponent alloys where the phase diagram is nonlinear and the liquidus/solidus surfaces are curved, the partition coefficients are not constant. Instead, they depend on the local composition of the alloy at the interface:

$$k_J = k_J\left(C_1^l, \ldots, C_N^l\right), \quad J \in [1, N].$$

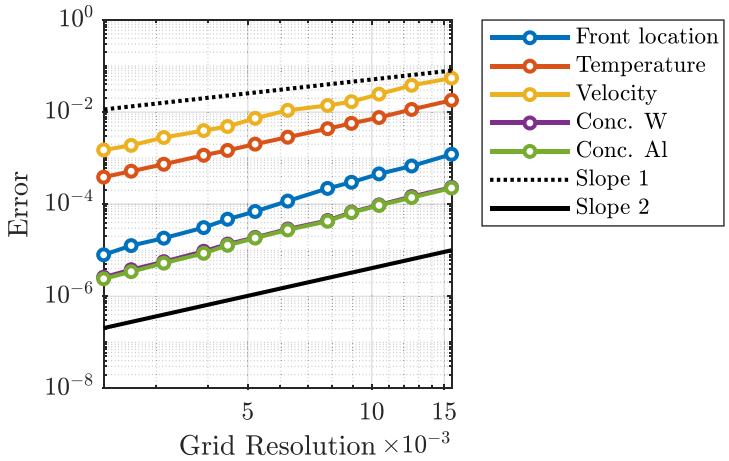

Figure 10. Overall accuracy of the computational method in the case of stable axisymmetric solidification. Figure reprinted from [70], Copyright (2023), with permission from Elsevier.

Mass conservation of each species at the moving interface further imposes a set of interfacial boundary conditions known as the solute-rejection equations. These conditions ensure that the solute flux in the liquid and the rate of incorporation (or rejection) of solute into the solid phase are consistent:

$$D_J^l \partial_{\boldsymbol{n}_l} C_J^l - (1-k_J)\, v_{\boldsymbol{n}} C_J^l = 0, \quad \boldsymbol{x} \in \Gamma(t), \quad J \in [1,N], \tag{10}$$

where D_J^l denotes the diffusivity of species J in the liquid phase. These equations capture the complex coupling between solute transport, interface motion, and phase equilibrium, and are essential for predicting microsegregation, solute trapping, and morphological stability during solidification of multicomponent alloys. Once the normal velocity at the interface is defined, the level-set evolution equation is solved as described in section 2. We refer the interested reader to [70] for the details of the numerical implementation and to [143] for a coupling of simulation of a pure substance with fluid flows.

3.2. Level-set simulations

A detailed accuracy analysis of the temperature, concentration, interface velocity, and interface location was conducted in [70] and is shown in figure 10 for a ternary Co–W–Al solidification case. Errors are measured in the L^∞-norm over the full simulation time, capturing the worst-case deviation from the reference solution. The results indicate convergence rates approaching second order. This is particularly important in multicomponent alloy solidification, where strong thermal and solutal gradients interact with a moving interface. The verified accuracy supports the model's reliability for predictive simulations of complex solidification phenomena.

A practical simulation of directional solidification of a ternary Co–W–Al system is given in figure 11. Denoting the computational domain Ω, with boundary $\partial\Omega$, it is assumed that the total heat flux is specified and the boundary is impermeable to solutes:

$$\begin{aligned} \lambda^\nu \partial_{\boldsymbol{n}_\nu} T^\nu &= g_{T^\nu}, & \boldsymbol{x} &\in \Omega^\nu \cap \partial\Omega, & \nu &= s,l, \\ D_J^l \partial_{\boldsymbol{n}_l} C_J^l &= 0, & \boldsymbol{x} &\in \Omega^l \cap \partial\Omega, & J &\in [1,N], \end{aligned} \tag{11}$$

where $g_{T^\nu} = g_{T^\nu}(t,\boldsymbol{x})$, $\nu = s,l$, are prescribed heat fluxes for the liquid and solid phases. The simulation investigates the influence of the thermal gradient G and the diffusion coefficient of aluminum (Al) on dendritic growth during solidification. As expected, increasing the thermal gradient leads to finer dendritic structures. The qualitative dependence of dendrite arm spacing on both G and the solidification rate R is consistent with observations in binary alloy systems. However, the quantitative details, such as the coefficients and exponents in the scaling laws, may differ due to additional complexities inherent in multicomponent systems. These include the presence of nontrivial phase diagrams, cross-diffusion effects (e.g. Onsager coupling), and unequal solute diffusivities in the liquid phase. The level-set simulation framework is particularly well-suited to capturing these effects, enabling systematic studies of how they influence microstructural evolution.

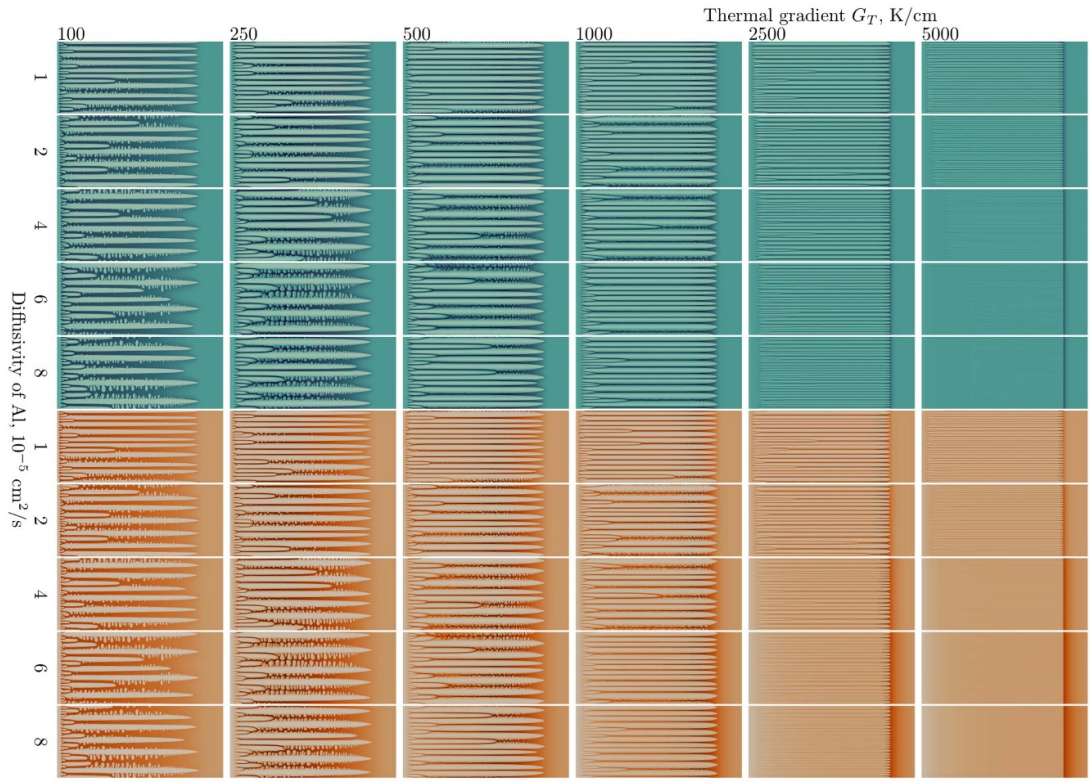

Figure 11. Solidification microstructures obtained for values of Al diffusivity from $D^{\text{Al}} = 10^{-5}$ cm^2 s^{-1} to $8 \cdot 10^{-5}$ cm^2 s^{-1} and G_T from 100 K cm^{-1} to 5000 K cm^{-1} in case of $L = 0.05$ cm and $V = 0.01$ cm s^{-1}. Displayed in color is the concentration field of Al and W. Figure reprinted from [70], Copyright (2023), with permission from Elsevier.

4. Application—epitaxial growth and the IDM

4.1. The IDM

In [85, 86], Caflisch *et al* introduced the IDM as well as its numerical approximation using the level-set method in [87, 144] and later analyzed the IDM and developed step edge boundary conditions for well-posedness [145]. The core idea of the IDM is to represent the boundary of atomic-height islands using a continuous level-set function $\phi(\boldsymbol{x}, t)$, such that Islands of heights k are represented by the level sets $\phi(\boldsymbol{x}, t) = k - 1$, and to consider a mean-field adatom density $\rho = \rho(\boldsymbol{x}, t)$. As such, the IDM achieves atomistic fidelity in the growth direction, while employing a continuum description in the lateral directions. The method also accounts for nucleation events, and other atomistic processes influencing island growth. The level-set function evolves according to the transport equation:

$$\frac{\partial \phi}{\partial t} + v_n |\nabla \phi| = 0,$$

where v_n is the interface normal velocity field, which is computed from the adatom fluxes across the island boundary from the upper $^{(k+1)}$ and lower terraces $^{(k)}$:

$$v_n = aD \left(\boldsymbol{n} \cdot \nabla \rho^{(k+1)} - \boldsymbol{n} \cdot \nabla \rho^{(k)} \right),$$

where D is the adatom diffusion coefficient and a is the lattice constant.

The adatom concentration $\rho(\boldsymbol{x}, t)$ satisfies a reaction-diffusion equation with source and sink terms:

$$\frac{\partial \rho}{\partial t} = F + D\nabla^2 \rho - \frac{\mathrm{d}N_{\text{nuc}}}{\mathrm{d}t},$$

where F is the deposition flux and the last term models the nucleation rate of new dimers assuming a probability proportional to $\langle \rho^2 \rangle$, i.e. the integral of ρ^2, and written as:

$$\frac{\mathrm{d}N_{\text{nuc}}}{\mathrm{d}t} = 2D\sigma_1 \langle \rho^2 \rangle,$$

where σ_1 is the capture number for nucleation [146]. The factor of 2 accounts for the capture of 2 adatoms during nucleation and the fact that dimers are assumed to be stable. In [147, 148], it was established that the capture numbers σ_s associated with islands of size s obey the scaling relation $\sigma_s/\sigma_{av} = L(s/s_{av})$, where L denotes a linear functional dependence. This representation provides a consistent framework in which the reference value σ_1 may be prescribed explicitly. This stochastic nucleation mechanism has been validated using KMC simulations [149]. Anisotropic growth can be captured by modifying v_n. A key advantage of the IDM is its ability to take large time steps while accurately capturing the essential physics of adatom diffusion and detachment. A notable application of this approach is presented in [150], where an IDM was employed to study the narrowing and sharpening of the island-size distribution as a function of strain in the submonolayer heteroepitaxial growth regime. In that work, the model is coupled to an elastic formulation based on atomistic interactions, which is solved efficiently at each simulation step.

The diffusion equation governing the adatom density ρ requires the specification of appropriate boundary conditions at island boundaries to accurately describe the underlying atomistic processes. These boundary conditions play a critical role in determining the predictive capabilities of the IDM, as they directly influence mass transport at the evolving interface. In the case where the diffusion from the upper and lower terraces are equal, the boundary condition is $\rho = \rho_{\text{eq}}$, where ρ_{eq} denotes the equilibrium adatom density. However, for most epitaxial growth, the diffusion coefficients are not equal, which promotes the growth of mounds with important practical applications in photonic-crystal lasers, quantum dot lasers, single-photon emitters, solar cells, catalytic converters, lithography, and more. This boundary condition encapsulates the influence of the Ehrlich–Schwoebel (ES) barrier [151, 152] and serves as a key element in bridging atomistic-scale kinetics with continuum-scale morphological evolution [153–155]:

$$\nabla\rho \cdot \boldsymbol{n} + \frac{D'}{D - D'}\rho = \frac{D'}{D - D'}\rho_{\text{eq}}, \tag{12}$$

where ρ and its gradient $\nabla\rho$ are evaluated at the island boundary, D' is an atomistic rate that characterizes the energy barrier for adatom diffusion across the island edge and $\boldsymbol{n}$ is the outward normal to the boundary. In the limit $D' \to D$, the boundary condition (12) simplifies to the Dirichlet condition $\rho(\mathbf{x}) = \rho_{\text{eq}}$, as found in classical theories of step-flow growth [71, 156, 157]. The equilibrium adatom density ρ_{eq} plays a central role in defining attachment kinetics at step edges. In [158], an expression for ρ_{eq} is derived under the assumption of no Ehrlich–Schwoebel barrier, while in [137], the authors develop and implement a formulation that incorporates the effects of a finite Ehrlich–Schwoebel barrier. More generally, the value of ρ_{eq} depends on atomistic kinetic parameters, including the detachment rate and the rate of edge diffusion, as discussed in [85].

4.2. Level-set simulation

As an illustrative example, we report the results of level-set simulations from [159]. In the case of irreversible aggregation, corresponding to the boundary condition $\rho = 0$ at island edges, the IDM yields results that are in good agreement with KMC simulations, as shown in [87]. Figure 12 illustrates this agreement by showing the evolution of the adatom density and island density as functions of surface coverage for various values of the ratio D/F. Additionally, the cluster size distribution at a final coverage of 20% is presented, further demonstrating the consistency between the IDM and atomistic simulation results. Level-set simulations have been used to find the functional form of capture numbers used in rate equations expressing the densities of islands of all sizes. The capture numbers quantify the efficiency with which an island of a given size, in a specified environment, competes for available monomers. A key advantage of the Island Density Model is its implicit incorporation of island-island correlations, thereby accounting for the geometric arrangement of islands relative to their neighbors. Notably, the capture numbers were found to exhibit a linear dependence on island size [147, 148, 160].

Figure 13 illustrates the influence of the step-edge barrier on surface morphology during epitaxial growth. For a strong Ehrlich–Schwoebel barrier, corresponding to a small ratio $D'/D = 0.01$, the simulation exhibits the formation of well-defined mounds with a characteristic 'wedding cake' structure, featuring approximately ten exposed terraces after the deposition of eleven monolayers. As D'/D increases, reflecting a reduction in the strength of the Ehrlich–Schwoebel barrier, the mounding becomes less pronounced. In the case where $D'/D = 0.95$, which is a very high ratio, the surface evolves toward a morphology consistent with near layer-by-layer growth, indicating that the suppression of interlayer transport asymmetry promotes smoother film evolution.

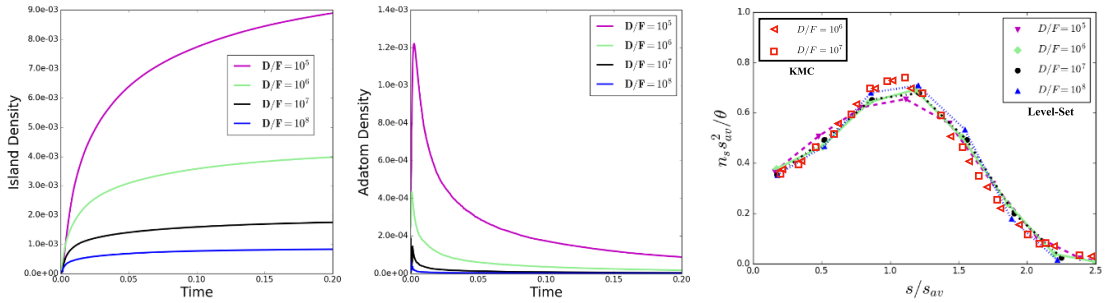

Figure 12. The island density (left) and adatom density (center) and cluster size distribution (right) for different values of D/F in the case of the boundary condition $\rho = 0$ (irreversible aggregation). Each simulation has a final coverage of 20%. The results of the KMC simulations are from [87]. Figure reprinted from [159], Copyright (2018), with permission from Elsevier.

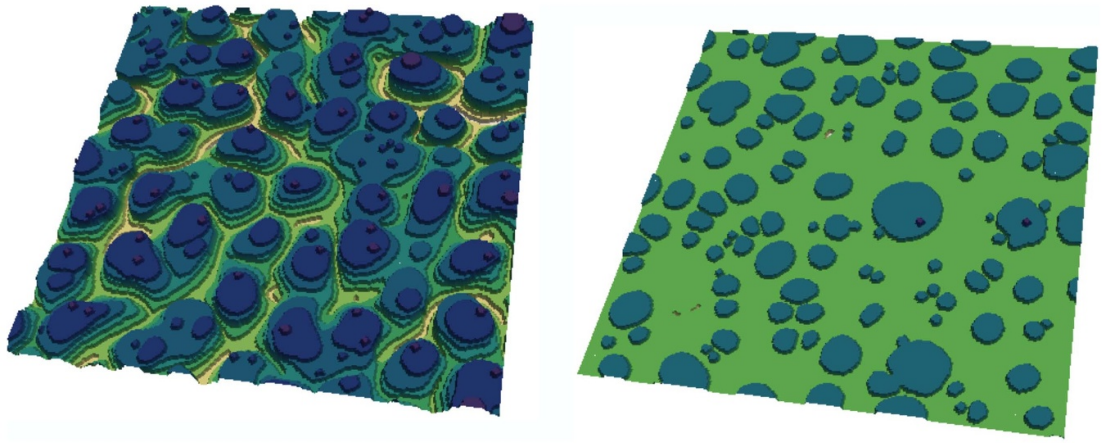

Figure 13. Effects of the Ehrlich–Schwoebel barrier and formation of mounds with $D'/D = 0.01$ (left) corresponding to a strong Ehrlich–Schwoebel barrier and $D'/D = 0.95$ (right), corresponding to a scenario close to $\rho(\mathbf{x}) = \rho_{\text{eq}}$. Both simulations are at the same times. Figure reprinted from [159], Copyright (2018), with permission from Elsevier.

5. Conclusion and perspective

The level-set method has emerged as a unifying computational framework for modeling free boundary problems across a wide spectrum of materials science applications. This review has synthesized its role in two contrasting yet complementary contexts: the solidification of multicomponent alloys and the mesoscale dynamics of epitaxial growth. In both application, the method's ability to maintain a sharp interface, naturally handle topological changes, and flexibly incorporate boundary conditions provides significant advantages over alternative approaches.

For alloy solidification, particularly in the context of AM, the level-set formulation enables high-fidelity simulations of solid–liquid interfaces, capturing complex thermodynamic interactions and multi-species transport with high accuracy. It accommodates multicomponent systems and sharp-interface physics that are beyond the reach of phase-field models, especially for more than three component alloys. In the context of epitaxial growth, the IDM and its level-set implementation offers a continuum-scale alternative to stochastic KMC simulations, dramatically reducing computational cost while preserving physical accuracy. It efficiently models nucleation, coalescence, and step-edge kinetics, with the flexibility to incorporate key phenomena such as the Ehrlich–Schwoebel barrier through Robin-type boundary conditions. Taken together, these applications underscore the versatility and robustness of level-set methods in materials science. Their seamless integration with finite volume and finite difference discretizations, AMR, and physically grounded boundary conditions makes them a powerful tool for predictive modeling and design.

Further developments in multiscale coupling, uncertainty quantification, and high-performance implementations will continue to expand the frontiers of level-set-based simulation in materials science. An especially promising direction is the integration of machine learning (ML) with level-set frameworks

in materials science for designing hybrid physics-based/data-driven simulations. ML can assist in learning surrogate models for expensive forward simulations, accelerating inverse design by providing data-driven approximations of the shape-to-structure map. Recent advances in computational materials science have explored this integration to enhance modeling capabilities, improve computational efficiency, and enable data-driven materials design. One such effort is the Level-Set Learning framework, which employs reversible neural networks to identify low-dimensional parameterizations of level sets in high-dimensional spaces. This approach has proven especially effective for reducing uncertainties and avoiding overfitting when working with limited data in inverse design and predictive modeling applications [161]. Another direction is the use of hybrid inference systems that couple ML with classical numerical techniques to improve curvature estimation in level-set computations or the evolution of the level-set itself. By using neural networks to refine gradient and curvature evaluations near interfaces, this approach helps mitigate numerical errors such as mass loss and surface tension computations, thereby increasing the accuracy of multiphase and interface-driven simulations [162–165].

ML techniques have also been integrated into the level-set framework to address Stefan problems [166], and have also been employed for operator learning in the context of inverse problems governed by diffusion-dominated dynamics [167] on fixed irregular domains. The physics-informed neural network (PINN) approach of [166] to the solution of the Stefan problem showed success on the prediction of planar interfaces, but it is not clear whether or not this approach will be accurate in the practical cases where dendritic structures develop. In addition, [168] pointed out that the erratic convergence behavior often observed in PINNs may stem from their reliance on automatic differentiation. This concern is further supported by [169], which highlights fundamental flaws in software-based automatic differentiation, including its dependency on the network's current approximation of the solution during training. This dependency can lead to significant errors, particularly when the evolving solution is far from the true one. To address this issue, [168] proposed incorporating a discretized formulation of the governing PDE, thereby bypassing automatic differentiation. Their results demonstrated that convergence improves systematically with the introduction of additional virtual grid points, yielding more accurate and stable solutions. Other fundamental work on optimization of neural networks can be found in [170, 171] and the references therein. These examples collectively highlight the emerging role of ML as a powerful complement to level-set methods in addressing multiscale, nonlinear, and data-intensive challenges in materials science.

Data availability statement

The data cannot be made publicly available upon publication because the cost of preparing, depositing and hosting the data would be prohibitive within the terms of this research project. The data that support the findings of this study are available upon reasonable request from the authors.

Acknowledgments

Frederic Gibou was partially supported by NSF CBET-EPSRC 2054894 and ACS PRF 66673-ND9. Ron Fedkiw was partially by ONR N00014-24-1-2644, ONR N00014-21-1-2771, and ONR N00014-19-1-2285. Russel Caflisch was partially supported by KAUST ORFS-2023-OFP-5538.2. Stanley Osher was partially supported by ONR N00014-20-1-2787, NSF-2208272, STROBE NSF-1554564, NSF 234525 and by Air Force Office of Scientific Research (AFOSR) MURI FA9550-18-502.

Appendix. ENO–WENO schemes

We provide details on the ENO/WENO schemes used in this work

A.1. ENO schemes

In the numerical solution of Hamilton–Jacobi equations and conservation laws, one of the key challenges is to design reconstructions that remain accurate in smooth regions while avoiding spurious oscillations near discontinuities. The ENO schemes address this challenge and are built upon two guiding principles:

1. The upwind direction must be correctly identified,
2. When extending the stencil to construct higher-order interpolants, the additional point should be chosen from the region where the solution exhibits the greatest smoothness, thereby suppressing oscillations near discontinuities.

A convenient framework for constructing polynomial interpolants in the context of ENO reconstructions is provided by Newton's form together with divided difference tables. Consider, for example, a stencil consisting of the grid points x_0, x_1, x_2, and x_3. The Newton representation of the interpolating polynomial is given by:

$$\tilde{u}(x) = \underbrace{a_0}_{\tilde{u}_0(x)} + \underbrace{a_1(x-x_0)}_{\tilde{u}_1(x)} + \underbrace{a_2(x-x_0)(x-x_1)}_{\tilde{u}_2(x)} + \underbrace{a_3(x-x_0)(x-x_1)(x-x_2)}_{\tilde{u}_3(x)},$$

where the coefficients $a_i \in \mathbb{R}$ are found by imposing that:

$$\tilde{u}(x_0) = u(x_0), \quad \tilde{u}(x_1) = u(x_1), \quad \tilde{u}(x_2) = u(x_2), \quad \tilde{u}(x_3) = u(x_3).$$

With this polynomial, the derivative at x_i is expressed as:

$$\frac{\mathrm{d}\tilde{u}}{\mathrm{d}x}(x_i) = \tilde{u_1}(x_i) + \tilde{u_2}(x_i) + \tilde{u_3}(x_i).$$

The divided-difference table provides a convenient framework for defining the coefficients a_i iteratively. Since $\tilde{u}(x_0) = u(x_0)$, the first coefficient depends only on the initial data point[7], which we denote by

$$a_0 = u[x_0].$$

Once a_0 is known, the next coefficient a_1 is determined from the condition $\tilde{u}(x_1) = u(x_1)$, so that it depends on $u(x_0)$ and $u(x_1)$; we write

$$a_1 = u[x_0, x_1].$$

Proceeding in the same way, we obtain

$$a_2 = u[x_0, x_1, x_2], \qquad a_3 = u[x_0, x_1, x_2, x_3].$$

In general, the divided differences $u[\cdot]$ are defined recursively as

$$u[x_0, \ldots, x_i] = \frac{u[x_1, \ldots, x_i] - u[x_0, \ldots, x_{i-1}]}{x_i - x_0}.$$

The standard notations are $D^i u = u[x_0, \ldots, x_i]$

The divided differences are particularly useful because their magnitudes provide a measure of the local smoothness of the solution. Specifically, $|D^1 u|$ reflects the strength of the first derivative, $|D^2 u|$ that of the second derivative, and so forth. Consequently, they offer valuable guidance in selecting the most appropriate grid point to add to a stencil.

Third-order ENO (ENO3) reconstruction: In this work we employ the ENO3 scheme. Suppose that the characteristic direction is determined by λ. The construction of the interpolant proceeds as follows:
Step 1. Upwind selection. The first-order interpolant $\tilde{u}_1(x)$ must account for the upwind direction:

$$\tilde{u}_1(x) = \begin{cases} D^1_{i-\frac{1}{2}}, & \lambda \geqslant 0, \\ D^1_{i+\frac{1}{2}}, & \lambda < 0. \end{cases}$$

Step 2. Second-order extension. To avoid including discontinuities, the stencil is extended by comparing smoothness indicators. For instance, if $\lambda < 0$ the first step involves the points (x_i, x_{i+1}). The candidates for extension are x_{i-1}, associated with D^2_i, and x_{i+2}, associated with D^2_{i+1}. The second-order term is chosen as

$$\tilde{u}_2(x) = \begin{cases} D^2_i, & |D^2_i| \leqslant |D^2_{i+1}|, \\ D^2_{i+1}, & \text{otherwise.} \end{cases}$$

[7] Indeed, $a_0 = u(x_0)$.

Step 3. Third-order extension. The procedure is repeated at the third level. Suppose D_i^2 was selected at Step 2. The candidates are then x_{i-2} (associated with $D^3_{i-\frac{1}{2}}$) and x_{i+2} (associated with $D^3_{i+\frac{1}{2}}$). The third-order contribution is

$$\tilde{u}_3(x) = \begin{cases} D^3_{i-\frac{1}{2}}, & |D^3_{i-\frac{1}{2}}| \leqslant |D^3_{i+\frac{1}{2}}|, \\ D^3_{i+\frac{1}{2}}, & \text{otherwise.} \end{cases}$$

Interpolant and derivative. In this example, assuming $|D^3_{i-\frac{1}{2}}| \leqslant |D^3_{i+\frac{1}{2}}|$, the reconstructed polynomial is

$$\tilde{u}(x) \;=\; D_i^0 + D^1_{i+\frac{1}{2}}(x-x_i) + D_i^2(x-x_i)(x-x_{i+1}) + D^3_{i-\frac{1}{2}}(x-x_i)(x-x_{i+1})(x-x_{i-1}).$$

From this expression, the derivative at x_i follows directly:

$$\tilde{u}_x(x) \;=\; D^1_{i+\frac{1}{2}} + D_i^2\left[2x-(x_i+x_{i+1})\right] + D^3_{i-\frac{1}{2}}\left(3x^2 - 2x(x_i+x_{i-1}+x_{i+1}) + (x_{i-1}x_i + x_ix_{i+1} + x_{i-1}x_{i+1})\right).$$

Notation: In the case $\lambda > 0$, the upwind stencil involves the points i and $i-1$. We denote by $D_x^- u$ the corresponding approximation of $u_x(x_i)$. Conversely, when $\lambda < 0$, the upwind stencil involves the points i and $i+1$, and we denote by $D_x^+ u$ the approximation of $u_x(x_i)$.

A.2. WENO schemes

As described in appendix A.1, the ENO scheme selects among three candidate stencils, first by enforcing the correct upwind direction and then by avoiding stencils that cross discontinuities. In smooth regions, a weighted convex combination of these stencils yields higher-order accuracy. This principle forms the foundation of the WENO schemes.

We illustrate the construction for the approximation of $D_x^- u$; the case of $D_x^+ u$ follows analogously. The three possible ENO approximations of $D_x^- u$ are given by

$$\begin{aligned} u_x^1 &= \tfrac{1}{3}d_1 - \tfrac{7}{6}d_2 + \tfrac{11}{6}d_3, \\ u_x^2 &= -\tfrac{1}{6}d_2 + \tfrac{5}{6}d_3 + \tfrac{1}{3}d_4, \\ u_x^3 &= \tfrac{1}{3}d_3 + \tfrac{5}{6}d_4 - \tfrac{1}{6}d_5, \end{aligned}$$

where the finite differences are defined as

$$d_1 = \frac{u_{i-2}-u_{i-3}}{\Delta x}, \quad d_2 = \frac{u_{i-1}-u_{i-2}}{\Delta x}, \quad d_3 = \frac{u_i - u_{i-1}}{\Delta x}, \quad d_4 = \frac{u_{i+1}-u_i}{\Delta x}, \quad d_5 = \frac{u_{i+2}-u_{i+1}}{\Delta x}.$$

The WENO approximation of $D_x^- u$ is constructed as a convex combination of the above stencils:

$$D_x^- u \;=\; \omega_1 u_x^1 + \omega_2 u_x^2 + \omega_3 u_x^3, \tag{A.1}$$

where the nonlinear weights ω_k are chosen such that the scheme achieves fifth-order accuracy in smooth regions while retaining the ENO property near discontinuities. By construction, the weights satisfy $\omega_1 + \omega_2 + \omega_3 = 1$. The optimal (linear) weights that give fifth-order accuracy in smooth regions are $\{0.1, 0.6, 0.3\}$.

The nonlinear weights are obtained through the following procedure:

- **Smoothness indicators.** For each stencil, define

$$\begin{aligned} S_1 &= \tfrac{13}{12}(d_1 - 2d_2 + d_3)^2 + \tfrac{1}{4}(d_1 - 4d_2 + 3d_3)^2, \\ S_2 &= \tfrac{13}{12}(d_2 - 2d_3 + d_4)^2 + \tfrac{1}{4}(d_2 - d_4)^2, \\ S_3 &= \tfrac{13}{12}(d_3 - 2d_4 + d_5)^2 + \tfrac{1}{4}(3d_3 - 4d_4 + d_5)^2. \end{aligned}$$

- **Nonlinear coefficients.** Define

$$\begin{aligned} \alpha_1 &= \frac{0.1}{(S_1+\epsilon)^2}, \\ \alpha_2 &= \frac{0.6}{(S_2+\epsilon)^2}, \\ \alpha_3 &= \frac{0.3}{(S_3+\epsilon)^2}, \end{aligned}$$

with $\epsilon = 10^{-6}\max(d_1^2, d_2^2, d_3^2, d_4^2, d_5^2) + 10^{-99}$ to prevent division by zero.

- **Nonlinear weights.** Finally, set

$$\omega_1 = \frac{\alpha_1}{\alpha_1 + \alpha_2 + \alpha_3},$$
$$\omega_2 = \frac{\alpha_2}{\alpha_1 + \alpha_2 + \alpha_3},$$
$$\omega_3 = \frac{\alpha_3}{\alpha_1 + \alpha_2 + \alpha_3}.$$

The construction of $D_x^+ u$ follows in the same manner, but with the definitions of the finite differences shifted as

$$d_1 = \frac{u_{i+3} - u_{i+2}}{\Delta x}, \quad d_2 = \frac{u_{i+2} - u_{i+1}}{\Delta x}, \quad d_3 = \frac{u_{i+1} - u_i}{\Delta x}, \quad d_4 = \frac{u_i - u_{i-1}}{\Delta x}, \quad d_5 = \frac{u_{i-1} - u_{i-2}}{\Delta x}.$$

We refer the interested reader to [41, 43, 44] for additional details on ENO/WENO schemes.

ORCID iDs

Frederic Gibou 0000-0001-7022-5262
Ron Fedkiw 0009-0008-6853-2499
Russel Caflisch 0000-0003-3121-1188
Stanley Osher 0000-0002-7900-4658

References

[1] Osher S and Sethian J A 1988 Fronts propagating with curvature-dependent speed: algorithms based on Hamilton–Jacobi formulations *J. Comput. Phys.* **79** 12–49
[2] Sussman M, Smereka P and Osher S 1994 A level set approach for computing solutions to incompressible two-phase flow *J. Comput. Phys.* **114** 146–59
[3] Sussman M, Smith K M, Hussaini M Y, Ohta M and Zhi-Wei R 2007 A sharp interface method for incompressible two-phase flows *J. Comput. Phys.* **221** 469–505
[4] Sussman M, Fatemi E, Smereka P and Osher S 1998 An improved level set method for incompressible two-phase flows *Comput. Fluids* **27** 663–80
[5] Sussman M, Almgren A S, Bell J B, Colella P, Howell L H and Welcome M 1999 An adaptive level set approach for incompressible two-phase flows *J. Comput. Phys.* **148** 81–124
[6] Chang Y C, Hou T Y, Merriman B and Osher S 1996 A level set formulation of Eulerian interface capturing methods for incompressible fluid flows *J. Comput. Phys.* **124** 449–64
[7] Enright D, Nguyen D, Gibou F and Fedkiw R 2003 Using the particle level set method and a second order accurate pressure boundary condition for free surface flows *Proc. 4th ASME-JSME Joint Fluids Eng. Conf.* (ASME) p FEDSM2003–45144
[8] Hou T Y, Li Z, Osher S and Zhao H 1997 A hybrid method for moving interface problems with application to the hele–shaw flow *J. Comput. Phys.* **134** 236–52
[9] Udaykumar H S, Mittal R, Rampunggoon P and Khanna A 2001 A sharp interface Cartesian grid method for simulating flows with complex moving boundaries *J. Comput. Phys.* **174** 345–80
[10] Nguyen D, Gibou F and Fedkiw R 2002 A fully conservative ghost fluid method and stiff detonation waves *12th Int. Detonation Symp.* (*San Diego, CA*)
[11] Gibou F'eric and Min C 2012 Efficient symmetric positive definite second-order accurate monolithic solver for fluid/solid interactions *J. Comput. Phys.* **231** 3246–63
[12] Caiden R, Fedkiw R P and Anderson C 2001 A numerical method for two-phase flow consisting of separate compressible and incompressible regions *J. Comput. Phys.* **166** 1–27
[13] Ng Y T, Min C and Gibou F'eric 2009 An efficient fluid–solid coupling algorithm for single-phase flows *J. Comput. Phys.* **228** 8807–29
[14] Tasdizen T, Whitaker R, Burchard P and Osher S 2002 Geometric surface smoothing via anisotropic diffusion of normals *Proc. IEEE Visualization 2002 (VIS 2002)* (IEEE) pp 125–32
[15] Osher S and Paragios N 2003 *Geometric Level Set Methods in Imaging, Vision and Graphics* (Springer)
[16] Osher S and Tsai R 2003 Review article: level set methods and their applications in image science *Commun. Math. Sci.* **1** 1–20
[17] Guendelman E, Selle A, Losasso F and Fedkiw R 2005 Coupling water and smoke to thin deformable and rigid shells *ACM Trans. Graph. (SIGGRAPH Proc.)* **24** 973–81
[18] Enright D, Marschner S and Fedkiw R 2002 Animation and rendering of complex water surfaces *ACM Trans. Graph. (SIGGRAPH Proc.)* **21** 736–44
[19] Losasso F, Fedkiw R and Osher S 2006 Spatially adaptive techniques for level set methods and incompressible flow *Comput. Fluids* **35** 995–1010
[20] Foster N and Fedkiw R 2001 Practical animation of liquids *Proc. ACM SIGGRAPH 2001* pp 23–30
[21] Losasso F, Gibou F and Fedkiw R 2004 Simulating water and smoke with an octree data structure *ACM Trans. Graph. (SIGGRAPH Proc.)* pp 457–62
[22] Nguyen D Q, Fedkiw R P and Kang M 2001 A boundary condition capturing method for incompressible flame discontinuities *J. Comput. Phys.* **172** 71–98
[23] Aanjaneya M, Patkar S and Fedkiw R 2013 A monolithic mass tracking formulation for bubbles in incompressible flow *J. Comput. Phys.* **247** 17–61

[24] Burger M, Osher S J and Yablonovitch E 2004 Inverse problem techniques for the design of photonic crystals *IEICE Trans. Electron.* **87** 258–65
[25] Zhao H-K, Osher S and Fedkiw R 2001 Fast surface reconstruction using the level set method *Proc. IEEE Workshop on Variational and Level Set Methods in Computer Vision* (IEEE) pp 194–201
[26] Osher S J and Santosa F 2001 Level set methods for optimization problems involving geometry and constraints: I. Frequencies of a two-density inhomogeneous drum *J. Comput. Phys.* **171** 272–88
[27] Allaire G, Jouve F and Toader A-M 2002 A level-set method for shape optimization *C. R. Math.* **334** 1125–30
[28] Allaire G, Jouve F and Toader A-M 2004 Structural optimization using sensitivity analysis and a level-set method *J. Comput. Phys.* **194** 363–93
[29] Chowdhury R, Egan R, Bochkov D and Gibou F 2022 Efficient calculation of fully resolved electrostatics around large biomolecules *J. Comput. Phys.* **448** 110718
[30] Egan R and Gibou F 2018 Fast and scalable algorithms for constructing solvent-excluded surfaces of large biomolecules *J. Comput. Phys.* **374** 91–120
[31] Ouaknin G, Laachi N, Bochkov D, Delaney K, Fredrickson G and Gibou F 2017 Functional level-set derivative for self consistent field theory *J. Comput. Phys.* **345** 168–85
[32] Ouaknin G, Laachi N, Delaney K, Fredrickson G and Gibou F 2016 Shape optimization for DSA *Proc. SPIE* **9777** 168–78
[33] Ouaknin G, Laachi N, Delaney K, Fredrickson G H and Gibou F 2016 Self-consistent field theory simulations of polymers on arbitrary domains *J. Comput. Phys.* **327** 168–85
[34] Ouaknin G, Laachi N, Bochkov D, Delaney K, Fredrickson G H and Gibou F 2017 Functional level-set derivative for a polymer self consistent field theory Hamiltonian *J. Comput. Phys.* **345** 207–23
[35] Ouaknin G Y, Laachi N, Delaney K, Fredrickson G H and Gibou F 2018 Level-set strategy for inverse DSA-lithography *J. Comput. Phys.* **375** 1159–78
[36] Bochkov D and Gibou F 2024 A non-parametric gradient-based shape optimization approach for solving inverse problems in directed self-assembly of block copolymers *Commun. Appl. Math. Comput.* **6** 1472–89
[37] Burger M and Osher S J 2005 A survey on level set methods for inverse problems and optimal design *Eur. J. Appl. Math.* **16** 263–301
[38] Sussman M 2003 A second order coupled level set and volume-of-fluid method for computing growth and collapse of vapor bubbles *J. Comput. Phys.* **187** 110–36
[39] Sussman M and Puckett E G 2000 A coupled level set and volume-of-fluid method for computing 3D and axisymmetric incompressible two-phase flows *J. Comput. Phys.* **162** 301–37
[40] Enright D, Fedkiw R, Ferziger J and Mitchell I 2002 A hybrid particle level set method for improved interface capturing *J. Comput. Phys.* **183** 83–116
[41] Osher S and Fedkiw R 2002 *Level Set Methods and Dynamic Implicit Surfaces* (Springer)
[42] Sethian J A 1999 Evolving interfaces in computational geometry, fluid mechanics, computer vision and materials science *Level set Methods and Fast Marching Methods (Cambridge Monographs on Applied and Computational Mathematics)* vol 3, 2nd edn (Cambridge University Press)
[43] Osher S and Fedkiw R P 2001 Level set methods: an overview and some recent results *J. Comput. Phys.* **169** 463–502
[44] Gibou F, Fedkiw R and Osher S 2018 A review of level-set methods and some recent applications *J. Comput. Phys.* **353** 82–109
[45] Osher S, Fedkiw R and Piechor K 2004 Level set methods and dynamic implicit surfaces *Appl. Mech. Rev.* **57** B15
[46] Gu D D, Meiners W, Wissenbach K and Poprawe R 2012 Laser additive manufacturing of metallic components: materials, processes and mechanisms *Int. Mater. Rev.* **57** 133–64
[47] Pollock T M, Clarke A J and Babu S S 2020 Design and tailoring of alloys for additive manufacturing *Metall. Mater. Trans. A* **51** 6000–19
[48] Dutta B, Babu S and Jared B H 2019 *Science, Technology and Applications of Metals in Additive Manufacturing* (Elsevier)
[49] DebRoy T, Wei H L, Zuback J S, Mukherjee T, Elmer J W, Milewski J O, Beese A M, de Wilson-Heid A, De A and Zhang W 2018 Additive manufacturing of metallic components–process, structure and properties *Prog. Mater. Sci.* **92** 112–224
[50] Sames W J, List F A, Pannala S, Dehoff R R and Babu S S 2016 The metallurgy and processing science of metal additive manufacturing *Int. Mater. Rev.* **61** 315–60
[51] Das S, Bourell D L and Babu S S 2016 Metallic materials for 3D printing *MRS Bull.* **41** 729–41
[52] Raghavan N, Dehoff R, Pannala S, Simunovic S, Kirka M, Turner J, Carlson N and Babu S S 2016 Numerical modeling of heat-transfer and the influence of process parameters on tailoring the grain morphology of IN718 in electron beam additive manufacturing *Acta Mater.* **112** 303–14
[53] Kurz W, Bezencon C and Gäumann M 2001 Columnar to equiaxed transition in solidification processing *Sci. Technol. Adv. Mater.* **2** 185
[54] Reuther K and Rettenmayr M 2014 Perspectives for cellular automata for the simulation of dendritic solidification–a review *Comput. Mater. Sci.* **95** 213–20
[55] Karma A 2001 Phase-field formulation for quantitative modeling of alloy solidification *Phys. Rev. Lett.* **87** 115701
[56] Kim S G 2007 A phase-field model with antitrapping current for multicomponent alloys with arbitrary thermodynamic properties *Acta Mater.* **55** 4391–9
[57] Steinbach I 2009 Phase-field models in materials science *Modelling Simul. Mater. Sci. Eng.* **17** 073001
[58] Tan L and Zabaras N 2007 A level set simulation of dendritic solidification of multi-component alloys *J. Comput. Phys.* **221** 9–40
[59] Chen S, Merriman B, Osher S and Smereka P 1997 A simple level set method for solving Stefan problems *J. Comput. Phys.* **135** 8–29
[60] Udaykumar H S, Marella S and Krishnan S 2003 Sharp-interface simulation of dendritic growth with convection: benchmarks *Int. J. Heat Mass Transfer* **46** 2615–27
[61] Papac J, Helgadottir A, Ratsch C and Gibou F 2013 A level set approach for diffusion and Stefan-type problems with Robin boundary conditions on Quadtree/Octree adaptive Cartesian grids *J. Comput. Phys.* **233** 241–61
[62] Chen H, Min C and Gibou F 2007 A supra-convergent finite difference scheme for the Poisson and heat equations on irregular domains and non-graded adaptive Cartesian grids *J. Sci. Comput.* **31** 19–60
[63] Gibou F'eric, Fedkiw R, Caflisch R and Osher S 2003 A level set approach for the numerical simulation of dendritic growth *J. Sci. Comput.* **19** 183–99
[64] Yang Y and Udaykumar H S 2005 Sharp interface Cartesian grid method III: solidification of pure materials and binary solutions *J. Comput. Phys.* **210** 55–74

[65] Theillard M 2015 Frédéric Gibou and Tresa Pollock. A sharp computational method for the simulation of the solidification of binary alloys *J. Sci. Comput.* **63** 330–54
[66] Sethian J A and Strain J 1992 Crystal growth and dendritic solidification *J. Comput. Phys.* **98** 231–53
[67] Mayo A 1984 The fast solution of Poisson's and the biharmonic equations on irregular regions *SIAM J. Numer. Anal.* **21** 285–99
[68] Gibou F, Fedkiw R, Cheng Li-T and Kang M 2002 A second-order accurate symmetric discretization of the Poisson equation on irregular domains *J. Comput. Phys.* **176** 205–27
[69] Gibou F'eric and Fedkiw R 2005 A fourth order accurate discretization for the Laplace and heat equations on arbitrary domains, with applications to the Stefan problem *J. Comput. Phys.* **202** 577–601
[70] Bochkov D, Pollock T and Gibou F 2023 A numerical method for sharp-interface simulations of multicomponent alloy solidification *J. Comput. Phys.* **494** 112494
[71] Pimpinelli A and Villain J 1999 *Physics of Crystal Growth* (Cambridge University Press)
[72] Brune H 1998 Microscopic view of epitaxial metal growth: nucleation and aggregation *Surf. Sci. Rep.* **31** 121–229
[73] Cheimarios N, To D, Kokkoris G, Memos G and Boudouvis A G 2021 Monte Carlo and kinetic Monte Carlo models for deposition processes *Front. Phys.* **9** 631918
[74] Sakthinathan S, Meenakshi G A, Vinothini S, Yu C-L, Chen C-L, Chiu T-W and Vittayakorn N 2025 A review of thin-film growth, properties, applications and future prospects *Processes* **13** 587
[75] Caflisch R 2006 Multiscale modeling for epitaxial growth *Multiscale Modeling of Epitaxial Growth Processes* ed A Voigt (Birkhäuser) pp 55–108
[76] Vlachos D G 2005 A review of multiscale analysis: examples from systems biology, materials growth and other reacting systems *Chem. Eng. Sci.* **60** 7–16
[77] Venables J A, Spiller G D T and Hanbücken M 1984 Nucleation and growth of thin films *Rep. Prog. Phys.* **47** 399–459
[78] Evans J W, Thiel P A and Bartelt M C 2006 Morphological evolution during epitaxial thin film growth: formation of 2d islands and 3d mounds *Surf. Sci. Rep.* **61** 1–128
[79] Maksym P A 1988 Fast Monte Carlo simulation of MBE growth *Semicond. Sci. Technol.* **3** 594
[80] DeVita J P, Sander L M and Smereka P 2005 Multiscale kinetic Monte Carlo algorithm for simulating epitaxial growth *Phys. Rev. B* **72** 205421
[81] Battaile C C and Srolovitz D J 2002 Kinetic Monte Carlo simulation of chemical vapor deposition *Annu. Rev. Mater. Res.* **32** 297–319
[82] Reuter K and Scheffler M 2006 First-principles kinetic Monte Carlo simulations for heterogeneous catalysis: application to the co oxidation at RuO_2(110) *Phys. Rev. B* **73** 045433
[83] Jiang H and Hou Z 2015 Large-scale epitaxial growth kinetics of graphene: a kinetic Monte Carlo study *J. Chem. Phys.* **143** 084109
[84] Chen X, Zhang X and Ai W 2024 Kinetic Monte Carlo study on the effect of growth conditions on the epitaxial growth of 3C-SiC (0001) vicinal surface *J. Vac. Sci. Technol. A* **42** 01
[85] Caflisch R E, Gyure M F, Merriman B, Osher S, Ratsch C, Vvedensky D D and Zinck J J 1999 Island dynamics and the level set method for epitaxial growth *Appl. Math. Lett.* **12** 13
[86] Gyure M F, Ratsch C, Merriman B, Caflisch R E, Osher S, Zinck J J and Vvedensky D D 1998 Level-set methods for the simulation of epitaxial phenomena *Phys. Rev. E* **58** R6927–30
[87] Chen S, Merriman B, Kang M, Caflisch R E, Ratsch C, Cheng Li-T, Gyure M, Fedkiw R P, Anderson C and Osher S 2001 A level set method for thin film epitaxial growth *J. Comput. Phys.* **167** 475–500
[88] Shu C-W 1989 Efficient implementation of essentially non-oscillatory schemes, II *J. Comput. Phys.* **78** 32–78
[89] Shu C-W and Osher S 1989 Efficient implementation of essentially non-oscillatory shock capturing schemes II *J. Comput. Phys.* **83** 32–78
[90] Liu X-D, Osher S and Chan T 1996 Weighted essentially non-oscillatory schemes *J. Comput. Phys.* **126** 202–12
[91] Jiang G-S and Peng D 2000 Weighted ENO schemes for Hamilton-Jacobi equations *SIAM J. Sci. Comput.* **21** 2126–43
[92] Tsitsiklis J 1995 Efficient algorithms for globally optimal trajectories *IEEE Trans. Autom. Control* **40** 1528–38
[93] Sethian J 1999 Fast marching methods *SIAM Rev.* **41** 199–235
[94] Zhao H 2004 A fast sweeping method for eikonal equations *Math. Comput.* **74** 603–27
[95] Tsai Y-H, Cheng L-T and Osher S 2003 Fast sweeping algorithms for a class of Hamilton–Jacobi equations *SIAM J. Numer. Anal.* **41** 673–94
[96] Zhao H 2007 Parallel implementations of the fast sweeping method *J. Comput. Math.* **25** 421–9
[97] Detrixhe M, Gibou F and Min C 2013 A parallel fast sweeping method for the eikonal equation *J. Comput. Phys.* **237** 46–55
[98] Detrixhe M and Gibou F 2016 Hybrid massively parallel fast sweeping method for static Hamilton–Jacobi equations *J. Comput. Phys.* **322** 199–223
[99] Tsai Y-H R 2002 Rapid and accurate computation of the distance function using grids *J. Comput. Phys.* **178** 175–95
[100] Danielsson P-E 1980 Euclidean distance mapping *Comput. Graph. Image Process.* **14** 227–48
[101] Borgefors G 1986 Distance transformations in digital images *Comput. Vis. Graph. Image Process.* **34** 344–71
[102] Sussman M and Fatemi E 1999 An efficient, interface-preserving level set re-distancing algorithm and its application to interfacial incompressible fluid flow *SIAM J. Sci. Comput.* **20** 1165–91
[103] Min C 2010 On reinitializing level set functions *J. Comput. Phys.* **229** 2764–72
[104] Darbon J and Osher S 2016 Algorithms for overcoming the curse of dimensionality for certain Hamilton–Jacobi equations arising in control theory and elsewhere *Res. Math. Sci.* **3** 19
[105] Chow Y T, Darbon J, Osher S and Yin W 2017 Algorithm for overcoming the curse of dimensionality for time-dependent non-convex Hamilton–Jacobi equations arising from optimal control and differential games problems *J. Sci. Comput.* **73** 617–43
[106] Mirzadeh M, Guittet A, Burstedde C and Gibou F 2016 Parallel level-set methods on adaptive tree-based grids *J. Comput. Phys.* **322** 345–64
[107] Min C, Gibou F'eric and Ceniceros H D 2006 A supra-convergent finite difference scheme for the variable coefficient Poisson equation on non-graded grids *J. Comput. Phys.* **218** 123–40
[108] Min C and Gibou F 2007 A second order accurate level set method on non-graded adaptive Cartesian grids *J. Comput. Phys.* **225** 300–21
[109] Mirzadeh M, Theillard M and Gibou F 2011 A second-order discretization of the nonlinear Poisson Boltzmann equation over irregular geometries using non-graded adaptive cartesian grids *J. Comput. Phys.* **230** 2125–40

[110] Theillard M, Djodom L F, Vie J-L and Gibou F 2013 A second-order sharp numerical method for solving the linear elasticity equations on irregular domains and adaptive grids–application to shape optimization *J. Comput. Phys.* **233** 430–48
[111] Mirzadeh M, Theillard M, Helgadottir A, Boy D and Gibou F 2012 An adaptive, finite difference solver for the nonlinear Poisson-Boltzmann equation with applications to biomolecular computations *Commun. Comput. Phys.* **13** 150–73
[112] Helgadottir A and Gibou F 2011 A Poisson-Boltzmann solver on irregular domains with Neumann or Robin boundary conditions on non-graded adaptive grid *J. Comput. Phys.* **230** 3830–48
[113] Min C and Gibou F 2007 Geometric integration over irregular domains with application to level-set methods *J. Comput. Phys.* **226** 1432–43
[114] Guittet A, Theillard M and Gibou F 2015 A stable projection method for the incompressible Navier–Stokes equations on arbitrary geometries and adaptive quad/octrees *J. Comput. Phys.* **292** 215–38
[115] Guittet A, Poignard C and Gibou F 2017 A Voronoi interface approach to cell aggregate electropermeabilization *J. Comput. Phys.* **332** 143–59
[116] Gibou F, Min C and Fedkiw R 2013 High resolution sharp computational methods for elliptic and parabolic problems in complex geometries *J. Sci. Comput.* **54** 369–413
[117] Min C and Gibou F 2006 A second order accurate projection method for the incompressible Navier–Stokes equations on non-graded adaptive grids *J. Comput. Phys.* **219** 912–29
[118] Chen H, Min C and Gibou F 2009 A numerical scheme for the Stefan problem on adaptive Cartesian grids with supralinear convergence rate *J. Comput. Phys.* **228** 5803–18
[119] Burstedde C, Wilcox L C and Ghattas O 2011 p4est: scalable algorithms for parallel adaptive mesh refinement on forests of octrees *SIAM J. Sci. Comput.* **33** 1103–33
[120] Berger M and Colella P 1989 Local adaptive mesh refinement for shock hydrodynamics *J. Comput. Phys.* **82** 64–84
[121] Fedkiw R P, Aslam T, Merriman B and Osher S 1999 A non-oscillatory Eulerian approach to interfaces in multimaterial flows (the ghost fluid method) *J. Comput. Phys.* **152** 457–92
[122] Fedkiw R P, Marquina A and Merriman B 1999 An isobaric fix for the overheating problem in multimaterial compressible flows *J. Comput. Phys.* **148** 545–78
[123] Fedkiw R P 2002 Coupling an Eulerian fluid calculation to a Lagrangian solid calculation with the ghost fluid method *J. Comput. Phys.* **175** 200–24
[124] Fedkiw R P, Aslam T and Xu S 1999 The ghost fluid method for deflagration and detonation discontinuities *J. Comput. Phys.* **154** 393–427
[125] Liu X-D, Fedkiw R P and Kang M 2000 A boundary condition capturing method for Poisson's equation on irregular domains *J. Comput. Phys.* **160** 151–78
[126] English R E, Qiu L, Yu Y and Fedkiw R 2013 Chimera grids for water simulation *ACM SIGGRAPH/Eurographics Symp. on Computer Animation (SCA)*
[127] Guittet A, Lepilliez M, Tanguy S and Gibou F'eric 2015 Solving elliptic problems with discontinuities on irregular domains—the Voronoi interface method *J. Comput. Phys.* **298** 747–65
[128] Egan R and Gibou F 2020 xGFM: recovering convergence of fluxes in the ghost fluid method *J. Comput. Phys.* **409** 109351
[129] Bochkov D and Gibou F 2020 Solving elliptic interface problems with jump conditions on Cartesian grids *J. Comput. Phys.* **407** 109269
[130] Ng Y T, Chen H, Min C and Gibou F'eric 2009 Guidelines for Poisson solvers on irregular domains with Dirichlet boundary conditions using the ghost fluid method *J. Sci. Comput.* **41** 300–20
[131] Coco A and Russo G 2013 Finite-difference ghost-point multigrid methods on Cartesian grids for elliptic problems in arbitrary domains *J. Comput. Phys.* **241** 464–501
[132] Gallinato O and Poignard C 2017 Superconvergent Cartesian methods for Poisson type equations in 2D—domains *J. Comput. Phys.* **339** 412–31
[133] Gallinato O and Poignard C 2017 Superconvergent second order Cartesian method for solving free boundary problem for invadopodia formation *J. Comput. Phys.* **339** 412–31
[134] Jomaa Z and Macaskill C 2008 Numerical solution of the 2-D Poisson equation on an irregular domain with Robin boundary conditions *Proc. 14th Biennial Computational Techniques and Applications Conf.* vol 50 pp 1–10
[135] Jomaa Z and Macaskill C 2010 The Shortley-Weller embedded finite-difference method for the 3D Poisson equation with mixed boundary conditions *J. Comput. Phys.* **229** 3675–90
[136] Bouchon F and Peichl G H 2007 A second-order immersed interface technique for an elliptic Neumann problem *Numer. Methods Part. Differ. Equ.* **23** 400–20
[137] Papac J, Gibou F and Ratsch C 2010 Efficient symmetric discretization for the Poisson, heat and Stefan-type problems with Robin boundary conditions *J. Comput. Phys.* **229** 875–89
[138] Min C and Gibou F 2008 Robust second-order accurate discretizations of the multi-dimensional Heaviside and Dirac delta functions *J. Comput. Phys.* **227** 9686–95
[139] Egan R and Gibou F 2017 Geometric discretization of the multidimensional Dirac delta distribution with application to the poisson equation with singular source terms *J. Comput. Phys.* **346** 71–90
[140] Arias V, Bochkov D and Gibou F 2018 Poisson equations in irregular domains with Robin boundary conditions—solver with second-order accurate gradients *J. Comput. Phys.* **365** 1–6
[141] Johansen H and Colella P 1998 A Cartesian grid embedded boundary method for Poisson equation on irregular domains *J. Comput. Phys.* **147** 60–85
[142] Bochkov D and Gibou F 2019 Solving poisson-type equations with Robin boundary conditions on piecewise smooth interfaces *J. Comput. Phys.* **376** 1156–98
[143] Bayat E, Egan R, Bochkov D, Sauret A and Gibou F 2022 A sharp numerical method for the simulation of Stefan problems with convective effects *J. Comput. Phys.* **471** 111627
[144] Ratsch C, Gyure M F, Caflisch R E, Gibou F, Petersen M, Kang M, Garcia J and Vvedensk D D 2002 Level-set method for island dynamics in epitaxial growth *Phys. Rev. B* **65** 195403
[145] Caflisch R E and Li B 2003 Analysis of island dynamics in epitaxial growth of thin films *Multiscale Model. Simul.* **1** 150–71
[146] Bales G S and Chrzan D C 1994 Dynamics of irreversible island growth during submonolayer epitaxy *Phys. Rev. B* **50** 6057–67
[147] Gibou F, Ratsch C, Chen S, Gyure M and Caflisch R 2001 Rate equations and capture numbers with implicit island correlations *Phys. Rev. B* **63** 115401

[148] Gibou F, Ratsch C and Caflisch R 2003 Capture numbers in rate equations and scaling laws for epitaxial growth *Phys. Rev. B* **67** 155403
[149] Ratsch C, Gyure M F, Chen S, Kang M and Vvedensky D D 2000 Fluctuation and scaling in aggregation phenomena *Phys. Rev. B* **61** R10598
[150] Ratsch C, DeVita J and Smereka P 2009 Level-set simulation for the strain-driven sharpening of the island-size distribution during submonolayer heteroepitaxial growth *Phys. Rev. B* **80** 155309
[151] Ehrlich G and Hudda F 1966 Atomic view of surface self-diffusion: tungsten on tungsten *J. Chem. Phys.* **44** 1039
[152] Schwoebel R L and Shipsey E J 1966 Step motion on crystal surfaces *J. Appl. Phys.* **37** 3682–6
[153] Chernov A A 1961 The spiral growth of crystals *Sov. Phys.-Usp.* **4** 116–48
[154] Villain J 1991 Continuum models of crystal growth from atomic beams with and without desorption *J. Phys. I* **1** 19–42
[155] Jeong H-C and Williams E D 1999 Steps on surfaces: experiment and theory *Surf. Sci. Rep.* **34** 171–294
[156] Burton W K, Cabrera N and Frank F C 1951 The growth of crystals and the equilibrium structure of their surfaces *Phil. Trans. R. Soc. A* **243** 299–358
[157] Lu J, Liu J-G and Margetis D 2015 Emergence of step flow from an atomistic scheme of epitaxial growth in 1 + 1 dimensions *Phys. Rev. E* **91** 032403
[158] Caflisch R E, Weinan E, Gyure M F, Merriman B and Ratch C 1999 Kinetic model for a step edge in epitaxial growth *Phys. Rev. E* **59** 6879–87
[159] Mistani P, Guittet A, Bochkov D, Schneider J, Margetis D, Ratsch C and Gibou F 2018 The island dynamics model on parallel quadtree grids *J. Comput. Phys.* **361** 150–66
[160] Vvedensky D, Ratsch C, Gibou F and Vardavas R 2003 Singularities and spatial fluctuations in submonolayer epitaxy *Phys. Rev. Lett.* **90** 189601
[161] Oak Ridge National Laboratory 2022 Level set learning: reducing uncertainties in function approximation (available at: www.ornl.gov/research-highlight/level-set-learning-reducing-uncertainties-function-approximation)
[162] Ángel Larios-Cárdenas L and Gibou F'eric 2023 Machine learning algorithms for three-dimensional mean-curvature computation in the level-set method *J. Comput. Phys.* **478** 111995
[163] Ángel Larios-Cárdenas L and Gibou F 2022 A hybrid inference system for improved curvature estimation in the level-set method using machine learning *J. Comput. Phys.* **463** 111291
[164] Ángel Larios-Cárdenas L and Gibou F 2022 Error-correcting neural networks for semi-Lagrangian advection in the level-set method *J. Comput. Phys.* **471** 111623
[165] Ángel Larios-Cárdenas L and Gibou F 2021 A deep learning approach for the computation of curvature in the level-set method *SIAM J. Sci. Comput.* **43** A1754–79
[166] Wang S and Perdikaris P 2021 Deep learning of free boundary and Stefan problems *J. Comput. Phys.* **428** 109914
[167] Pakravan S, Mistani P A, Aragon-Calvo M A and Gibou F 2021 Solving inverse-PDE problems with physics-aware neural networks *J. Comput. Phys.* **440** 110414
[168] Mistani P A, Pakravan S, Ilango R and Gibou F 2023 JAX-DIPS: neural bootstrapping of finite discretization methods and application to elliptic problems with discontinuities *J. Comput. Phys.* **493** 112480
[169] Johnson D, Maxfield T, Jin Y and Fedkiw R 2023 Software-based automatic differentiation is flawed (arXiv:2305.03863)
[170] Johnson D and Fedkiw R 2024 Addressing discontinuous root-finding for subsequent differentiability in machine learning, inverse problems and control *J. Comput. Phys.* **497** 112624
[171] Hyde D, Bao M and Fedkiw R 2021 On obtaining sparse semantic solutions for inverse problems, control and neural network training *J. Comput. Phys.* **443** 110498